Integrating Aeroelastic and Primary Flight Control: Robust Design and Wind Tunnel Demonstration

Felix Stalla*
German Aerospace Center (DLR), 82234 Weßling, Germany
Delft University of Technology, Delft, 2629HS, The Netherlands

Gertjan Looye†
German Aerospace Center (DLR), 82234 Weßling, Germany

Manuel Pusch ‡
Munich University of Applied Sciences, 80335 Munich, Germany

Spilios Theodoulis §
Delft University of Technology, Delft, 2629HS, The Netherlands

Aeroelastic control functions, such as active gust load alleviation, enable lighter structural designs for future commercial aircraft and thereby support reductions in fuel consumption and emissions. Traditionally, these functions are developed separately, as add-ons to the primary flight control system, relying on a clear frequency separation between rigid-body and flexible aircraft dynamics. As aircraft structures become more flexible, this separation no longer holds, resulting in coupled dynamics and motivating an integrated design. This paper presents an integrated control law design using μ-synthesis robust control, a powerful method that allows for efficient trade-offs between multiple performance and robustness objectives. The design jointly addresses gust load alleviation as an aeroelastic control function and command augmentation as a primary flight control function. Controller performance is validated through wind tunnel experiments on a flexible, clamped wing. Although this setup prevents direct testing of primary flight control functions, representative tasks are defined to enable meaningful experimental validation. Wind tunnel results demonstrate the effectiveness of the integrated control law.

I. Introduction

Aeroelastic control functions become increasingly important as next-generation transport aircraft incorporate slender, highly flexible structures to reduce weight and improve efficiency [1, 2]. These functions aim to actively shape and stabilize the aircraft's flexible response, thereby mitigating adverse aeroelastic phenomena such as dynamic instabilities (e.g. flutter) and high structural loads induced by maneuvering and atmospheric disturbances, including gusts and turbulence. While active flutter suppression has recently found first applications on commercial aircraft, load alleviation functions have a long operational history, from early applications on the Lockheed L-1011 to modern airliners such as the Boeing 787 and Airbus A350 [3]. Traditionally, aeroelastic control functions are designed separately and subsequently integrated as add-ons to an existing (primary) flight control architecture [4, 5].

Primary flight control (PFC) focuses on controlling the flight dynamics of the aircraft and is typically realized in a cascaded control architecture [6–8], schematically shown in Fig. 1. The outermost loop provides guidance and trajectory commands, while the intermediate loop regulates flight path and speed. This loop generates attitude commands for the innermost loop, the attitude control system. Pilot control inputs act directly on the attitude loop, which is why the outer loops are indicated by dashed lines. The attitude control loop can be realized using various control architectures and design methods, but in all cases it serves as a stability and command augmentation system (SCAS). This system provides reference tracking, disturbance rejection, and ensures stability, with the help of feedforward and feedback control. The resulting commands are then allocated to the available control surfaces, which produce the desired aircraft response.

*Research Associate, Institute of Aeroelasticity, Department Control of Aeroelastic Systems, felix.stalla@dlr.de;
also: Delft University of Technology, Faculty of Aerospace Engineering, Control & Simulation Section, j.f.stalla@tudelft.nl.
†Department Head, Institute of Aeroelasticity, Department Control of Aeroelastic Systems, gertjan.looye@dlr.de, AIAA Member.
‡Professor, Department of Mechanical Engineering, Automotive Engineering, and Aerospace Engineering, manuel.pusch@hm.edu.
§Associate Professor, Faculty of Aerospace Engineering, Control & Simulation Section, s.theodoulis@tudelft.nl, AIAA Associate Fellow.

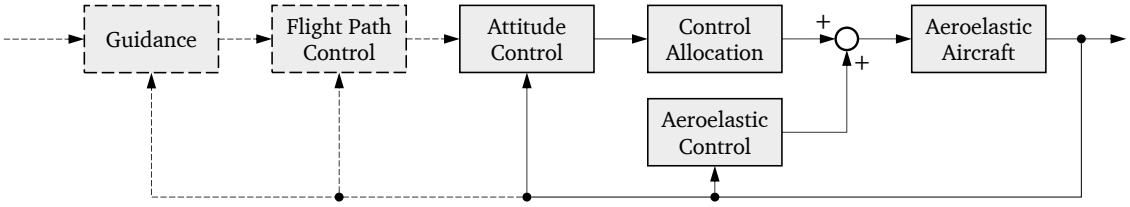

Fig. 1 Schematic of a classical cascaded flight control architecture.

In the classical flight control architecture shown in Fig. 1, aeroelastic control functions are designed separately and integrated at the control allocation level [4, 5]. This approach relies on the assumption that PFC and aeroelastic control functions address inherently different dynamics (rigid-body versus flexible aircraft structure), with well-separated frequency ranges. Filtering is used to ensure that each control law operates within its designated frequency band, minimizing cross-coupling effects. However, as aircraft become increasingly flexible, the assumption of clear frequency separation between rigid-body and flexible dynamics no longer holds [9]. The dynamics become coupled, rigid and flexible eigenmodes move closer together in frequency, and aeroelastic effects become relevant at low frequencies. In such cases, a separate design becomes impractical, as numerous iterations are required to address emerging cross-couplings and dependencies. This motivates the development of integrated control laws.

Figure 2 schematically illustrates how an integrated controller replaces the separate functions of the classical architecture. The integrated controller unifies attitude control in form of a SCAS with aeroelastic control functions, control allocation, and sensor allocation. By integrating all four tasks within the innermost control loop, the coupled rigid-body and flexible dynamics can be addressed simultaneously, while jointly optimizing the usage of available control authority and sensor information to meet both primary flight and aeroelastic control objectives. This improves overall control system performance.

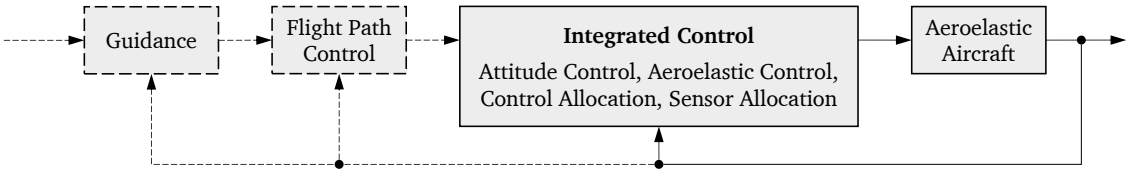

Fig. 2 Schematic of an integrated flight control architecture.

Multiple integrated controller designs are proposed in literature. In [9], a multi-objective parameter optimization is used to design an integrated controller combining primary flight control, load alleviation, and flutter control, i.e. a fixed structure controller is optimized to meet design criteria. Alternatively, [10] uses an eigenstructure assignment and a linear-quadratic regulator (LQR) approach to achieve longitudinal flight control combined with aeroelastic stabilization. In [11], robust control in form of $\mathcal{H}_\infty$-closed-loop shaping is applied to combine a stability augmentation system with aeroelastic damping augmentation, and [12] extends this approach to a linear parameter-varying (LPV) design.

This paper employs μ-synthesis robust control [13–16] to design integrated control laws that combine stability and command augmentation (SCAS) with gust load alleviation (GLA). Robust control is well suited to integrated design, as the objectives of the different functions can be formulated within a joint optimization framework using weighting functions, without prescribing a fixed controller structure. This is particularly advantageous for aeroelastic aircraft with a large number of sensors and control surfaces, where actuator-sensor pairings are not as obvious as in conventional PFC. The resulting unstructured synthesis enables the controller to optimally exploit available sensors and actuators while enforcing performance objectives and control and sensor allocation constraints through the chosen weighting functions. In addition, robustness is a key requirement to ensure reliable controller performance in the presence of uncertainty. The μ-synthesis framework offers separate means to impose performance and robustness requirements, thereby facilitating more systematic control-law design [17].

Two integrated control laws are designed, representing longitudinal and lateral motion: load factor tracking combined with active GLA, and roll command tracking combined with active GLA. A structured approach to realize these integrated control laws using μ-synthesis is described. The application case is a flexible wing tested in a wind tunnel, enabling experimental evaluation of the controllers. The wind tunnel setup imposes significant physical constraints on the implementable PFC functions. The wing is clamped at it's root, thus rigid-body motion cannot occur, and rigid-body

feedback quantities are not available. This paper details how a meaningful experimental validation of the control laws can still be achieved by reformulating the PFC tasks into equivalent ones that can be realized in the wind tunnel.

The paper is structured as follows. Section II introduces the aeroelastic modeling framework and the derivation of a control-oriented model for the flexible wing used as the application case. Section III defines the control objectives, including the reformulation of representative primary flight control tasks for implementation in the wind tunnel environment. Section IV presents the μ-synthesis-based control law design method, translating control objectives into a generalized plant with weighting functions, and modeling uncertainty. Finally, Section V experimentally evaluates the designed integrated controllers in the wind tunnel.

II. Aeroelastic Modeling

To design an integrated inner-loop controller, a numerical model of the aeroservoelastic aircraft is required. The model is based on the equations of motions (EOM) in mean-axis formulation, as introduced in [18] and detailed in [19]. This formulation couples rigid-body and flexible dynamics using only the loads on the right hand side. Modeling is conducted in the VarLoads environment [20, 21], further details on the underlying equations are given in [22]. Since this paper focuses exclusively on the inner-loop dynamics, the translational and rotational kinematics are not considered.

A. Coupled Rigid-Body and Flexible Equations of Motion

Based on the mean-axis formulation, and under assumptions of a flat and non-rotating earth, uniform gravity, constant mass and inertia tensor, the rigid-body EOM can be defined as [18, 19, 22]:

$$\begin{bmatrix} m_b \cdot (\dot{\boldsymbol{V}}_b + \boldsymbol{\Omega}_b \times \boldsymbol{V}_b - \boldsymbol{T}_{bE} \cdot \boldsymbol{g}_E) \\ \boldsymbol{J}_b \cdot \dot{\boldsymbol{\Omega}}_b + \boldsymbol{\Omega}_b \times (\boldsymbol{J}_b \cdot \boldsymbol{\Omega}_b) \end{bmatrix} = \boldsymbol{\Phi}_{gb}^{\mathrm{T}} \cdot \boldsymbol{P}_g^{\mathrm{ext}}. \tag{1}$$

The EOM are defined in the aircraft body-fixed frame with respect to the center of gravity (index b). Linear momentum dynamics are described using the translational velocity vector $\boldsymbol{V}_b = [u_b, v_b, w_b]^T$. Angular momentum dynamics use the vector $\boldsymbol{\Omega}_b = [p_b, q_b, r_b]^T$ of rotational velocity, defined as roll, pitch and yaw rate. The aircraft mass is defined as m_b, the inertia tensor as $\boldsymbol{J}_b$. Gravity $\boldsymbol{g}_E$ is given in an earth-centered-earth-fixed frame and transformed to the aircraft frame. External loads, i.e. forces and moments, are defined as $\boldsymbol{P}_g^{\mathrm{ext}}$ on the right-hand side of the equation, mapped from the structural points (index g) to the center of gravity by the eigenvector matrix $\boldsymbol{\Phi}_{gb}$. These loads stem from aerodynamics and propulsion, and establish the link to the flexible EOM being defined as [19, 22]:

$$\boldsymbol{M}_{ff} \cdot \ddot{\boldsymbol{u}}_f + \boldsymbol{B}_{ff} \cdot \dot{\boldsymbol{u}}_f + \boldsymbol{K}_{ff} \cdot \boldsymbol{u}_f = \boldsymbol{\Phi}_{gf}^T \cdot \boldsymbol{P}_g^{\mathrm{ext}}. \tag{2}$$

In the flexible EOM, structural matrices for mass $\boldsymbol{M}_{ff}$, damping $\boldsymbol{B}_{ff}$, and stiffness $\boldsymbol{K}_{ff}$ are defined in the modal domain (index f), with $\boldsymbol{\Phi}_{gf}$ being the eigenvector matrix mapping external forces and moment from the structural points to the modal definition. The vector $\boldsymbol{u}_f$ and its derivatives capture the deformation, velocity and acceleration of the related (undampened) structural eigenmodes [23, 24]. A model truncation is performed to reduce model size, meaning only a limited number of eigenmodes are being considered [25].

The quantities on the left-hand side of these two equations of motions are obtained from numerical models such as finite element models [26]. The external loads on the right-hand side can be divided into propulsive and aerodynamic forces ($\boldsymbol{P}_g^{\mathrm{prop}}$, $\boldsymbol{P}_g^{\mathrm{aero}}$), while gravity is already accounted for on the left-hand side. Aerodynamic forces are calculated by applying the doublet lattice method (DLM) [27, 28] on the discretized aircraft. The aerodynamic forces can be caused by a rigid-body motion $\boldsymbol{u}_b$, a flexible motion $\boldsymbol{u}_f$, a control surface motion $\boldsymbol{u}_x$, or an atmospheric disturbance such as a gust w^{G}. This leads to the sum of external forces and moments being defined as:

$$\boldsymbol{P}_g^{\mathrm{ext}} = \boldsymbol{P}_g^{\mathrm{aero}} + \boldsymbol{P}_g^{\mathrm{prop}}, \qquad \boldsymbol{P}_g^{\mathrm{aero}} = f(\boldsymbol{u}_b, \boldsymbol{u}_f, \boldsymbol{u}_x, w^{\mathrm{G}}). \tag{3}$$

B. Actuators, Sensors, and Load Recovery

To complete the aeroservoelastic loop, the aeroelastic model of Eqs. 1 through 3 is augmented with models of actuators and sensors. Actuators can often be modeled as first or second order linear transfer functions which are augmented with time delay and nonlinearities. These include deflection, rate, and acceleration limits, backlash, and freeplay [29, 30]. The first or second order linear transfer function is denoted $\boldsymbol{G}_{\mathrm{act}}$, and time delay can be written in linear form using a Padé approximation of n-th order, yielding:

$$\boldsymbol{u}_x = e^{-s\cdot T_{\mathrm{act,i}}} \cdot \boldsymbol{I}_x \cdot \boldsymbol{G}_{\mathrm{act}} \cdot \boldsymbol{u}_{x,\mathrm{cmd}} \qquad \text{with} \quad e^{-s\cdot T_{\mathrm{act,i}}} \approx \frac{\left(1 - T_{\mathrm{act,i}}/2n \cdot s\right)^n}{\left(1 + T_{\mathrm{act,i}}/2n \cdot s\right)^n}. \tag{4}$$

Sensor dynamics are typically very fast, a detailed modeling is not performed here. Instead, sensors are modeled as a rigid-body spline mapping from the modal acceleration (index f) to a physical acceleration (index m) at the respective locations, with addition of a time delay in form of a Padé approximation, like for the actuators. This leads to:

$$\boldsymbol{y}_{\mathrm{acc}} = e^{-s\cdot T_{\mathrm{acc,i}}} \cdot \boldsymbol{I}_m \cdot \boldsymbol{T}_{mg} \cdot \boldsymbol{\Phi}_{gf} \cdot \ddot{\boldsymbol{u}}_f \qquad \text{with} \quad e^{-s\cdot T_{\mathrm{acc,i}}} \approx \frac{\left(1 - T_{\mathrm{acc,i}}/2n \cdot s\right)^n}{\left(1 + T_{\mathrm{acc,i}}/2n \cdot s\right)^n}. \tag{5}$$

Besides the acceleration captured by the sensors, another quantity is important when developing aeroelastic control functions: the loads at the structural grid points (index g). These can be obtained through application of the force summation method (FSM) [22, 31] based on the external loads from Eq. 3 and inertial acceleration from Eq. 2:

$$\boldsymbol{P}_g^{\mathrm{FSM}} = \boldsymbol{P}_g^{\mathrm{ext}} - \boldsymbol{P}_g^{\mathrm{iner}} = \boldsymbol{P}_g^{\mathrm{ext}} - \boldsymbol{M}_{gg} \cdot \boldsymbol{\Phi}_{gf} \cdot \ddot{\boldsymbol{u}}_f. \tag{6}$$

C. Application to the Flexible Wing Wind Tunnel Model

The general description of the aeroelastic model is now applied to the wind tunnel experiment that serves as an environment for controller validation. In this experiment a clamped flexible wing is excited by gusts generated upstream, as introduced further below in Section V. A schematic of the wind tunnel model indicating available sensors and control surfaces is given in Fig. 3.

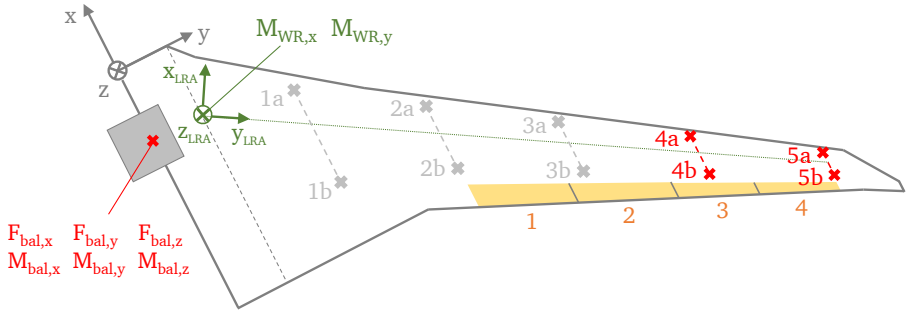

Fig. 3 Sensors, control surfaces, and loads on the aeroelastic wind tunnel model.

When applying the modeling framework to the wind tunnel wing, the most important difference is the clamping of the model that prevents the rigid-body motion of Eq. 1. Only an angle-of-attack can be set by adjusting the turning table on which the model is mounted. The lack of rigid-body dynamics in the wind tunnel poses a challenge when testing primary flight control implementations, a solution is being proposed in Section III. For now, only the flexible dynamics of Eq. 2 are being modeled. The modal mass, damping, and stiffness matrix are obtained from a finite element model. The external forces and moments of Eq. 3 stem only from aerodynamics generated on the flexible wing. The structural properties (flexible eigenfrequencies) of the model are summarized in Table 1. A detailed overview on how to identify aeroservoelastic parameters of such a flexible model is given in [30, 32].

The wing features four trailing-edge flaps, all powered by the same type of actuator. The actuator is modeled as presented in Eq. 4, employing a first order linear transfer function, time delay, and limitations on deflection and rate, all given in Table 1. The high roll-off frequency and rate limit are a result of scaling in the wind tunnel model and associated manufacturing constraints, which significantly rises the flexible eigenfrequency and thus calls for very fast actuators. In a full aircraft the properties would be adapted accordingly. Four z-directional acceleration sensors (4a, 4b, 5a, 5b) are available near the wing tip, modeled as in Eq. 5. Other acceleration sensors located more inboard will not be used here. The acceleration signals exhibit low dead-time and satisfactory noise properties, as indicated in the Table. The wing is mounted on a balance that is able to capture the forces and moment at the wing's root. The balance loads are included in the model by applying the force summation method of Eq. 6, with the innermost structural grid point resembling the balance. Figure 3 shows the coordinate system in which the balance forces and moments are defined.

Table 1 Model parameters of the flexible wing.

Domain	Parameter	Symbol	Value	Remark
structure	1st flex. eigenfreq.	$f_{\text{eig},1}$	8.5 Hz	out-of-plane bending
	2nd flex. eigenfreq.	$f_{\text{eig},2}$	36.5 Hz	out-of-plane bending
actuator	roll-off frequency	$\omega_{0,\text{act}}$	14.5 Hz	first order model
	dead time	T_{act}	6.0 ms	first order Padé
	deflection limit	$\delta_{\max}$	±15°	-
	rate limit	$\dot{\delta}_{\max}$	$\pm 1130°/s$	-
sensor	noise std. deviation	σ_{n}	0.75 m/s²	with actuators on
	dead time	T_{acc}	1.0 ms	first order Padé

Based on the model ingredients, a nonlinear simulation model is developed for validation, while a linear state-space model is used for control law design. The inputs of the state-space model are the commanded control surface deflection $\boldsymbol{u}_{x,\text{cmd}}$ and a one-dimensional gust signal $w^{\text{G}}(t)$ as disturbance, outputs are the acceleration sensor $\boldsymbol{y}_{\text{acc}}$ and feedback signals from the wind tunnel balance $\boldsymbol{y}_{\text{bal}}$ (here: vertical force and roll moment). Additionally, performance outputs are defined, which will be useful for controller synthesis. For GLA a suitable choice are the wing-root bending moment $M_{\text{WR,x}}$ and wing-root torsion moment $M_{\text{WR,y}}$, as discussed in Section III. These quantities are not identical to the measurements of the wind tunnel balance, since the coordinate system of the balance is oriented as indicated in Fig. 3, while the wing-root moments are captured in the coordinate system of the loads reference axis (LRA), also indicated in Fig. 3. The LRA follows the sweep of the wing. The state-space system is of the following form, and can naturally be converted into a plant transfer function $\boldsymbol{G}$:

$$\boldsymbol{G}: \quad \left[\begin{array}{c} \dot{\boldsymbol{x}} \\ \hdashline \boldsymbol{y} \\ \boldsymbol{p} \end{array}\right] = \left[\begin{array}{c|cc} \boldsymbol{A} & \boldsymbol{B}_u & \boldsymbol{B}_d \\ \hdashline \boldsymbol{C}_y & \boldsymbol{D}_{yu} & \boldsymbol{D}_{yd} \\ \boldsymbol{C}_p & \boldsymbol{D}_{pu} & \boldsymbol{D}_{pd} \end{array}\right] \cdot \left[\begin{array}{c} \boldsymbol{x} \\ \hdashline \boldsymbol{u} \\ \boldsymbol{d} \end{array}\right] \qquad \begin{aligned} \boldsymbol{u} &= \boldsymbol{u}_{x,\text{cmd}}, & \boldsymbol{d} &= w^{\text{G}}, \\ \boldsymbol{y} &= [\boldsymbol{y}_{\text{bal}}, \boldsymbol{y}_{\text{acc}}], & \boldsymbol{p} &= \boldsymbol{y}_{\text{WR,5:6}}, \end{aligned} \tag{7}$$

where both balance loads and wing-root loads are obtained from applying the FSM introduced in Eq. 6, such that the acceleration sensor output $\boldsymbol{y}_{\text{acc}}$ is augmented by:

$$\begin{aligned} \boldsymbol{y}_{\text{bal}} &= \boldsymbol{P}_{\text{bal}} = \boldsymbol{P}_{g,0}^{\text{FSM}} = [F_{\text{bal,x}}\ F_{\text{bal,y}}\ F_{\text{bal,z}};\ \ M_{\text{bal,x}}\ M_{\text{bal,y}}\ M_{\text{bal,z}}], \\ \boldsymbol{y}_{\text{WR}} &= \boldsymbol{P}_{\text{WR}} = \boldsymbol{P}_{g,1}^{\text{FSM}} = [F_{\text{WR,x}}\ F_{\text{WR,y}}\ F_{\text{WR,z}};\ \ M_{\text{WR,x}}\ M_{\text{WR,y}}\ M_{\text{WR,z}}]. \end{aligned} \tag{8}$$

All state-space matrices are dependent on the operating conditions. The wind tunnel test is conducted at a freestream velocity of U_∞ = 30 m/s. Pressure, density, and temperature are at sea-level atmospheric conditions. Having defined the state-space system, the transfer functions can be investigated to gain some insight into the behavior of the flexible wing. Exemplary, Fig. 4 shows the maximum singular values from either a gust input w^{G} (amplitude scaled to 1°) or all four control surfaces $\boldsymbol{u}_x$ (deflection scaled to 10°) to the vertical force at the balance $F_{\text{bal,z}}$, the wing-root bending moment $M_{\text{WR,x}}$, and the four outer acceleration sensors $\boldsymbol{y}_{\text{acc}}$.

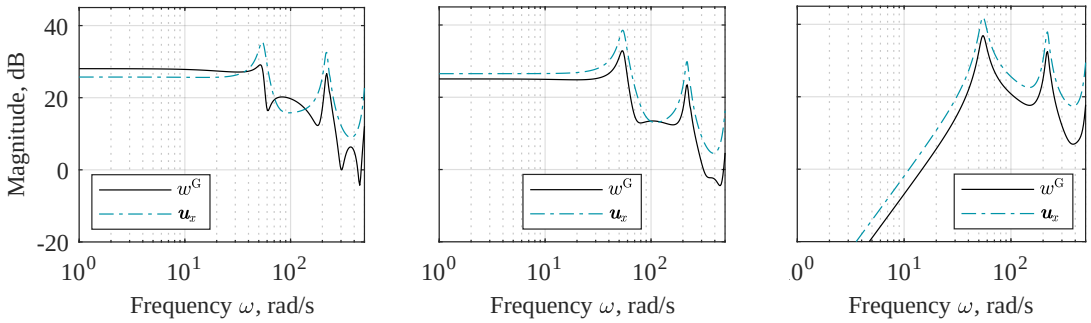

(a) Vertical force at balance $F_{\text{bal,z}}$ **(b) Bending moment $M_{WR,x}$** **(c) Acceleration $\boldsymbol{y}_{\text{acc}}$**

Fig. 4 Max. singular values from gust and control surfaces to balance force, wing-root moment, and acceleration.

All figures show a distinct peak at the eigenfrequency of the first flexible mode, at about 55 rad/s, 8.75 Hz, for a freestream velocity of 30 m/s. This mode is an out-of-plane bending of the wing. The second mode appears at about 220 rad/s or 35 Hz, also out-of-plane bending. For GLA, the primary task will be to dampen the first mode, while the second and higher order mode are already beyond the bandwidth of the actuators, see Table 1. Since the first bending mode is clearly visible in all sensors, it is well observable. Additionally, the figures reveal similar singular value magnitudes for the gust with 1° amplitude and the control surfaces deflected to a value of 10°. This suggests sufficient control authority to influence the dynamics of the flexible wing.

III. Control Objectives and Realization in the Wind Tunnel

The aim of this study is to investigate concepts for an integrated controller design for a flexible transport aircraft. Reference tracking and disturbance rejection for PFC is combined with gust disturbance rejection within the inner loop of a cascaded control architecture, see Fig. 2. On a full-scale aircraft, linear acceleration and angular velocity (see Eq. 1) can be measured using onboard accelerometers and gyroscopes, and are commonly selected as inner loop feedback variables in PFC. In this work, two representative tasks are considered: (i) load factor n_z command tracking (associated with the body-axis acceleration w_b) for longitudinal motion, and (ii) roll rate p_b command tracking for lateral motion. The experimental application however is not a full-scale aircraft but a wind tunnel setup featuring a clamped flexible wing, as described in Section II. This configuration imposes physical constraints on the implementation of PFC. In particular, the absence of rigid-body motion implies that neither linear acceleration nor angular velocity are useful to measure. Consequently, the aforementioned control tasks must be reformulated into equivalent, experimentally realizable tasks in the wind tunnel.

A. Load Factor Tracking by Means of Direct Lift in the Wind Tunnel

Based on the translational rigid-body dynamics of Eq. 1, the vertical acceleration $\dot{w}_b$ in z-direction can be extracted, and allows to define the load factor n_z as:

$$\begin{aligned} \dot{w}_b &= \dot{\boldsymbol{V}}_{b,z} = \frac{1}{m_b} \cdot F_{b,z}^{\text{ext}} + (\boldsymbol{T}_{bE} \cdot \boldsymbol{g}_E - \boldsymbol{\Omega}_b \times \boldsymbol{V}_b)_z, \\ n_z &= \frac{F_{b,z}^{\text{ext}}}{m_b \cdot g_{b,z}} = \frac{\dot{w}_b - g_{b,z} + (p_b \cdot v_b - q_b \cdot u_b)}{g_{b,z}}, \end{aligned} \tag{9a}$$

where the external force in z-direction $F_{b,z}^{\text{ext}}$ is composed of aerodynamic and propulsive forces. In a full-scale aircraft the load factor is determined by measuring the specific force $\dot{w}_b - g_{b,z}$ (see [33]), and then applying Eq. 9a. Such a measurement is not available in the wind tunnel. To define a representative tracking task for the experiment, several factors have to be considered. First, the wind tunnel model is clamped and therefore does not allow for a pitch or roll rate, hence the last term of Eq. 9a is not present. Second, since the wing is rotated by 90°, the gravity does not act notably. Third, a measurable quantity is the force in z-direction at the wing's root, $F_{\text{bal,z}}$, see Fig. 3. However, this does not match with the external force $F_{b,z}^{\text{ext}}$ in Eq. 9a. There are no propulsive forces, and only limited inertia forces, i.e. the interplay between aerodynamic and inertial forces cannot be fully reconstructed. Also, the tests are conducted on only one wing, such that for the entire aircraft the aerodynamic force will be approximately twice as high, plus the contribution from fuselage and empennage. Last, a representative mass must be defined, scaled to the wind tunnel size. Following these considerations, the alternative load factor for the wind tunnel can be defined as:

$$n_{\text{z,WT}} \approx \frac{2 \cdot F_{\text{bal,z}}}{m_{WT} \cdot g} = k_{nz} \cdot F_{\text{bal,z}}, \tag{9b}$$

with m_{WT} being a representative mass, not the actual weight of the wing model. Hence, the representative load factor tracking task is a vertical force $F_{\text{bal,z}}$ tracking task, with feedback provided by the balance.

The tracking task shall be realized in form of a direct lift control function. In direct lift the load factor can be directly controlled by control surfaces on the wing, opposed to classical longitudinal control, where an elevator deflection changes the angle-of-attack of the aircraft, hence it's lift, and thus the load factor. This improves the responsiveness of the control, as no pitch-up of the entire aircraft is needed, but lift is directly produced by adopting the camber of the wing. The trailing-edge control surfaces of the flexible wing with sufficiently fast dynamics (see Section II) allow to validate such a direct lift function experimentally.

B. Roll Command Tracking in the Wind Tunnel

Inspecting the rotational dynamics of Eq. 1, the second equation yields a relation for the pitch acceleration $\dot{p}_b$, with the simplified version in the second line assuming no pitch and yaw rate during the roll motion:

$$\begin{aligned} \dot{p}_b &= \dot{\boldsymbol{\Omega}}_{b,y} = [\boldsymbol{J}_b^{-1} \cdot (\boldsymbol{M}_b^{\text{ext}} - \boldsymbol{\Omega}_b \times (\boldsymbol{J}_b \cdot \boldsymbol{\Omega}_b))]_y, \\ \dot{p}_b &\approx \frac{1}{J_{xx}J_{zz} - J_{xz}^2} \cdot (J_{zz} \cdot M_{b,x}^{\text{ext}} + J_{zx} \cdot M_{b,z}^{\text{ext}}). \end{aligned} \tag{10a}$$

In a full-scale aircraft, roll rate p_b measurements would be available, allowing to control this rate directly. In the wind tunnel, such a roll rate measurement is not available. The best representative signal is the roll moment measured at the wind tunnel balance, labeled $M_{\text{bal,x}}$ in Fig. 3. This is not the same as the external roll moment $M_{\text{b,x}}^{\text{ext}}$ in Eq. 10a above, as there are no propulsive effects, and flexible inertia loads and gravity are not well represented. Because yaw moments cannot be reproduced in the wind tunnel, roll-yaw coupling is not present. Moreover, the inertial tensor can only be approximated with a representative quantity, labeled $J_{WT,xx}$. Finally, since only one wing is present this would imply an identical aerodynamic force from left and right wing on a full aircraft. With:

$$\dot{p}_{\text{WT}} \approx \frac{1}{J_{\text{WT,xx}}} \cdot 2 \cdot M_{\text{bal,x}} = k_p \cdot M_{\text{bal,x}}, \tag{10b}$$

the representative roll command tracking task is a roll moment $M_{\text{bal,x}}$ tracking task. Note that if the roll rate instead of the roll acceleration shall be tracked, this can be achieved by defining a constant, linking roll rate and acceleration.

C. Control Objectives of the Integrated Controller

The above defined representative tasks for primary flight control functions are to be combined with gust load alleviation in the integrated controller. The task of GLA will be to reduce the loads induced at the wing-root, the junction between wing and fuselage, as these loads are a key driver of structural weight. As described in the modeling Section II, wing-root bending and torsion moment are suitable quantities to include in the control synthesis. The task of GLA can be regarded as a desired increase in damping of the first flexible eigenmode, reducing the peak in wing-root loads as depicted in Fig. 4b. Now, the control objectives for the integrated controller can be defined. There are six main objectives with sub-objectives. The listed control objectives are conflicting, therefore the design scheme in Section IV will try to find the best compromise between these objectives.

1. Performance: primary flight control
   i. track a desired reference in the low frequency regime,
      here implemented: load factor (vertical force) and roll acceleration (roll moment) tracking,
   ii. reject disturbances when tracking the reference and attenuate noise in the high frequency range.
2. Performance: aeroelastic control
   i. reduce the gust-induced integral loads at the wing root: bending and torsion moment,
   ii. work for the entire range of gust gradients defined as well as other atmospheric disturbances.
3. Control activity
   i. minimize the required control activity,
   ii. obey restrictions in maximum deflection and rate,
   iii. distribute the PFC and GLA tasks to appropriate control surfaces.
4. Sensors
   i. determine usage of the sensors in the respective frequency ranges,
   ii. noise attenuation in the high frequency regime.
5. Stability
   i. nominal stability of the closed-loop system,
   ii. (disk-based) gain and phase margins of the nominal system.
6. Robustness
   i. achieve robust performance (requiring robust stability and nominal performance),
   ii. achieve robustness against uncertainties in the modeling, changing operating conditions and other deviations from the nominal condition.

IV. Integrated Control Law Design using μ-Synthesis

Based on the control objectives defined above, this section presents the design of an integrated control law providing combined PFC and GLA functionality. The aeroservoelastic system is characterized by rigid-body and flexible eigenmodes at distinct eigenfrequencies, motivating the use of a frequency-domain robust control approach [13, 14].

The design objective is to optimize robust performance [15], aiming to ensure closed-loop stability and performance not only in the nominal case, but also in the presence of uncertainties. In a multivariable (multiple input multiple output, MIMO) setting, this constitutes a challenging problem due to the simultaneous and potentially conflicting requirements on performance, control activity, sensors, nominal stability, and robustness, see Section III.C. In such cases, classical loop-shaping concepts based on singular values lose direct interpretability and may lead to overly conservative designs [17]. The structured singular value (SSV) μ [34] provides a scalar measure that captures these multiple objectives simultaneously. Building on this concept, μ-synthesis implemented via D-K iteration [15, 16] extends classical $\mathcal{H}_\infty$-closed-loop shaping [35] by iteratively adapting the synthesis model with scalings from intermediate μ-analyses [34, 36]. This enables direct optimization with respect to robust performance.

In μ-synthesis, the control design comprises two aspects, see [17]. First, requirements on performance, control activity, sensors, and nominal stability (objectives 1 through 5 in Section III.C) are enforced through the formulation of an appropriate generalized plant $\boldsymbol{P}$, in which relevant exogenous inputs and outputs are defined and weighted to shape the associated closed-loop transfer functions. For better readability, all these objectives are being referred to as *performance objectives*, as in [17]. Second, *robustness objectives* (objective 6 in Section III.C) are addressed by incorporating physically motivated structured uncertainties into the generalized plant, ensuring that all relevant plant variations are covered. These uncertainties arise from unknown or unmodeled dynamics, model mismatches, and variations in operating conditions. Using this setup, μ-synthesis then determines a controller that jointly satisfies the specified performance and robustness requirements in the presence of the defined uncertainties as good as possible. In this sense, when optimizing for robust performance using μ, the desired frequency-domain shaping is imposed not only on nominal closed-loop transfer functions, but on the set of transfer functions resulting from the uncertain plant [17].

In the following, μ-synthesis is applied to design two control laws. Inspiration is taken from [12]. The design follows the above introduced aspects to achieve the desired objectives. First, the overall control architecture is set. Second, *performance objectives* are translated by defining the generalized plant and selecting weighting functions. Third, *robustness objectives* are satisfied by modeling uncertainty based on physical insight. The control laws are:

1) Load factor tracking using direct lift, tracked variable $\boldsymbol{r}, \boldsymbol{y}_r : F_{\text{bal,z}} \simeq n_z$, wind tunnel balance vertical force, combined with gust load alleviation, using the additional feedback of the acceleration sensors $\boldsymbol{y}_{\text{acc}}$,
2) Roll command tracking, tracked variable $\boldsymbol{r}, \boldsymbol{y}_r : M_{\text{bal,x}} \simeq \dot{p}$, wind tunnel balance roll moment, combined with gust load alleviation, using the additional feedback of the acceleration sensors $\boldsymbol{y}_{\text{acc}}$.

A. Control Architecture

For the integrated controller a two degrees of freedom (DOF) architecture [13] is suggested, in which the controller receives both the reference signal $\boldsymbol{r}$ and feedback signal $\boldsymbol{y}$, rather than just the error between these signals. The controller $\boldsymbol{K}$ can be split into a feedback path $\boldsymbol{K}_y$ and a feedforward path $\boldsymbol{K}_r$. Feedback is well-suited for disturbance rejection, while feedforward shapes reference tracking. Figure 5 shows the proposed control structure, with the aeroservoelastic plant from Eq. 7 at its center. $\tilde{\boldsymbol{G}}$ indicates that an uncertain plant is incorporated, as discussed further below.

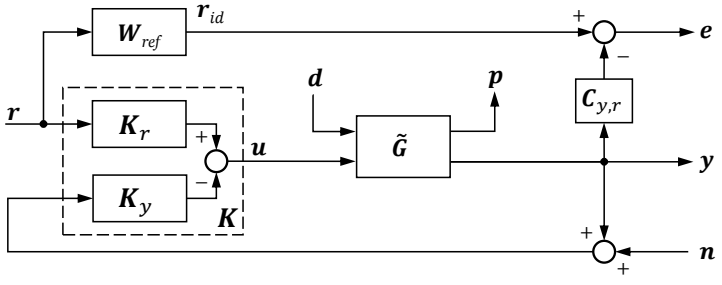

Fig. 5 Proposed control structure for the integrated controller.

Inputs to the closed-loop system are the reference signal $\boldsymbol{r} \in \mathbb{R}^{n_r}$, the gust $\boldsymbol{d} = w^{\text{G}} \in \mathbb{R}^{n_d}$, and the noise $\boldsymbol{n} \in \mathbb{R}^{n_y}$ in the feedback path. Outputs are the feedback variables $\boldsymbol{y} \in \mathbb{R}^{n_y}$, performance outputs $\boldsymbol{p} \in \mathbb{R}^{n_p}$, and the error $\boldsymbol{e} \in \mathbb{R}^{n_r}$.

Only the first $n_r \leq n_y$ feedback signals will be tracked, the other $n_y - n_r$ signals provide additional information. The error $\boldsymbol{e}$ is hence calculated between the ideal reference $\boldsymbol{r}_{id}$ and tracked feedback variables within $\boldsymbol{y}$, which are selected through the matrix $\boldsymbol{C}_{y,r} = \text{diag}(\boldsymbol{I}_{n_r}, \boldsymbol{0}_{n_y - n_r})$. This error can then be used to achieve performance for PFC tasks.

An implicit model-following approach is applied for reference tracking. The reference signal is filtered by a reference model $\boldsymbol{W}_{ref}$, defining the ideal tracking behavior, while the controller operates on the original reference signal. This formulation allows the (unstructured) control synthesis to determine the balance between feedforward and feedback paths without imposing a fixed structure. The approach supports various reference types: step, harmonic oscillation, or random excitation. If smooth references are expected from an outer loop (e.g. from the guidance system, Fig. 2), explicit model following might be more applicable. The reference model is designed as a first order low-pass:

$$\boldsymbol{W}_{ref} = \frac{\omega_{0,r}}{s + \omega_{0,r}} \cdot \boldsymbol{I}_{n_r}, \qquad \text{with} \quad \omega_{0,r} = 5 \text{ rad/s}. \tag{11}$$

The performance output $\boldsymbol{p}$ is used to fulfill GLA objectives. It includes both the wing-root bending and torsion moment, as presented in Section II and Eqs. 7 and 8. These quantities are not measurable, hence not available as feedback variables, but instead available as model-based quantities during the controller synthesis. This is, though unusual from a control perspective, characteristic for load alleviation functions. Feedback information is provided by the acceleration sensors, the untracked $n_y - n_r$ signals within $\boldsymbol{y}$.

From Fig. 5 the transfer functions of the closed-loop system are derived, that serve setting up the generalized plant in the subsequent section. Using the partitioned plant of Eq. 7, the input sensitivity function $\boldsymbol{S}_i = (\boldsymbol{I} + \boldsymbol{K}_y \boldsymbol{G}_{yu})^{-1}$, the output sensitivity $\boldsymbol{S}_o = (\boldsymbol{I} + \boldsymbol{G}_{yu} \boldsymbol{K}_y)^{-1}$, the input complementary sensitivity $\boldsymbol{T}_i = \boldsymbol{K}_y \boldsymbol{G}_{yu} \cdot \boldsymbol{S}_i$, and the output complementary sensitivity $\boldsymbol{T}_o = \boldsymbol{G}_{yu} \boldsymbol{K}_y \cdot \boldsymbol{S}_o$, can be defined for the feedback loop. Then, the transfer behavior is written as follows, where the selection matrix $\boldsymbol{C}_{y,r}$ for the error is omitted to improve readability, and the controller is partitioned into feedforward and feedback part as: $\boldsymbol{K} = \begin{bmatrix} \boldsymbol{K}_r & \boldsymbol{K}_y \end{bmatrix}$:

$$\begin{bmatrix} \boldsymbol{e} \\ \boldsymbol{u} \\ \boldsymbol{y} \\ \boldsymbol{p} \end{bmatrix} = \begin{bmatrix} \boldsymbol{W}_{ref} - \boldsymbol{S}_o \boldsymbol{G}_{yu} \boldsymbol{K}_r & -\boldsymbol{S}_o \boldsymbol{G}_{yd} & -\boldsymbol{T}_o \\ \boldsymbol{S}_i \boldsymbol{K}_r & -\boldsymbol{S}_i \boldsymbol{K}_y \boldsymbol{G}_{yd} & -\boldsymbol{K}_y \boldsymbol{S}_o \\ \boldsymbol{S}_o \boldsymbol{G}_{yu} \boldsymbol{K}_r & \boldsymbol{S}_o \boldsymbol{G}_{yd} & \boldsymbol{T}_o \\ \boldsymbol{G}_{pu} \boldsymbol{S}_i \boldsymbol{K}_r & \boldsymbol{G}_{pd} - \boldsymbol{G}_{pu} \boldsymbol{K}_y \boldsymbol{S}_o \boldsymbol{G}_{yd} & -\boldsymbol{G}_{pu} \boldsymbol{K}_y \boldsymbol{S}_o \end{bmatrix} \cdot \begin{bmatrix} \boldsymbol{r} \\ \boldsymbol{d} \\ \boldsymbol{n} \end{bmatrix}. \tag{12}$$

B. Generalized Plant and Weighting Functions for Performance Objectives

The performance objectives (objectives 1 through 5 in Section III.C) are enforced by shaping relevant closed-loop transfer functions, commonly referred to as sensitivity functions, defined in Eq. 12. This is accomplished by augmenting the aeroelastic plant $\boldsymbol{G}$ of Eq. 7 with appropriate scaling and weighting functions, resulting in the generalized plant $\boldsymbol{P}$ with exogenous inputs $\boldsymbol{w}$ and exogenous outputs $\boldsymbol{z}$. Within μ-synthesis, the $\mathcal{H}_\infty$-norm between these inputs and outputs will be minimized by optimizing the controller $\boldsymbol{K}$. For the integrated controllers designed here, each of the closed-loop inputs (reference, disturbance, noise) and outputs (tracking error, control activity, plant output, performance) will be penalized by a weighting function, as illustrated in the generalized plant depicted in Fig. 6. The closed-loop transfer functions (sensitivity functions) to be shaped are summarized in Table 2.

Inspired by [37], dynamic weights $\boldsymbol{W}$ will be defined on the output side to shape the frequency response, while static weights $\boldsymbol{V}$ will be defined on both the input and the output side to scale (and normalize) the signals appropriately. Dynamic weights are always defined about the 0 dB line, and static weights allow to adapt the magnitude. A classical normalization of the plant, see for example [13], is no longer required but included in the weights. The weighting imposed in the generalized plant can be summarized as:

$$\begin{bmatrix} \boldsymbol{z}_1 \\ \boldsymbol{z}_2 \\ \boldsymbol{z}_3 \\ \boldsymbol{z}_4 \end{bmatrix} = \begin{bmatrix} \boldsymbol{V}_e \boldsymbol{W}_e \cdot \boldsymbol{e} \\ \boldsymbol{V}_p \boldsymbol{W}_p \cdot \boldsymbol{p} \\ \boldsymbol{V}_u \boldsymbol{W}_u \cdot \boldsymbol{u} \\ \boldsymbol{V}_y \boldsymbol{W}_y \cdot \boldsymbol{y} \end{bmatrix}, \qquad \begin{bmatrix} \boldsymbol{r} \\ \boldsymbol{d} \\ \boldsymbol{n} \end{bmatrix} = \begin{bmatrix} \boldsymbol{V}_r \cdot \boldsymbol{w}_1 \\ \boldsymbol{V}_d \cdot \boldsymbol{w}_2 \\ \boldsymbol{V}_n \cdot \boldsymbol{w}_3 \end{bmatrix}. \tag{13}$$

In the following, these weighting functions are defined to shape the desired closed-loop transfer functions, linking to the performance objectives (performance, control activity, sensors, nominal stability). A summary is given in Table 2. The generalized plant in Fig. 6 also sees structured uncertainties included at the plant's input and output (dashed boxes), this will be discussed in Section IV.C in order to impose robustness objectives.

Table 2 Relevant closed-loop transfer functions and weights to shape these.

Objective	Sensitivity to shape		Tuning of	
	Name	Formula	Channel	Weights
Reference Tracking	Feedforward Sensitivity	$\boldsymbol{W}_{ref} - \boldsymbol{S}_o\boldsymbol{G}_{yu}\boldsymbol{K}_r$	Error z_1	$\boldsymbol{V}_r$, $\boldsymbol{V}_e\boldsymbol{W}_e$
Disturbance Rejection	Disturbance Sensitivity	$\boldsymbol{S}_o\boldsymbol{G}_{yd}$		$\boldsymbol{V}_d$, $\boldsymbol{V}_e\boldsymbol{W}_e$
Aeroelastic Performance	Performance Load Sensitivity	$\boldsymbol{G}_{pd} - \boldsymbol{G}_{pu}\boldsymbol{K}_y\boldsymbol{S}_o\boldsymbol{G}_{yd}$	Performance z_2	$\boldsymbol{V}_p\boldsymbol{W}_p$
Control Activity	Feedforward Control Sensitivity	$\boldsymbol{S}_i\boldsymbol{K}_r$	Control Activity z_3	$\boldsymbol{V}_u\boldsymbol{W}_u$
	Feedback Control Sensitivity	$\boldsymbol{K}_y\boldsymbol{S}_o$		
Sensor Usage	Complementary Sensitivity	$\boldsymbol{T}_o$	Output z_4	$\boldsymbol{V}_n$, $\boldsymbol{V}_y\boldsymbol{W}_y$
Nominal Stability				

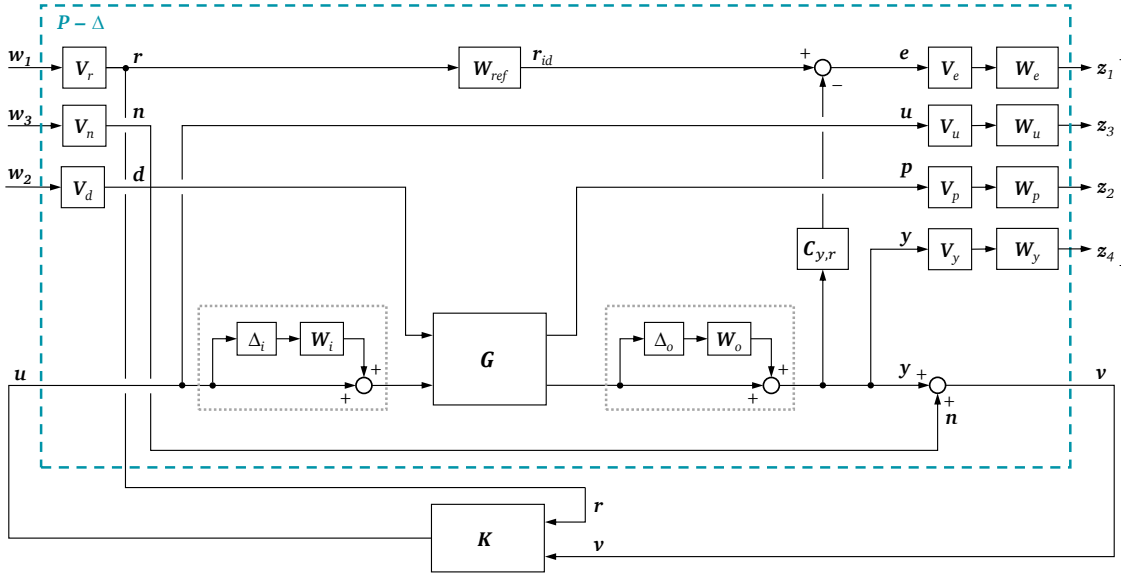

Fig. 6 Generalized plant for the integrated controller.

1. Error Weighting Function

The error channel is used to achieve reference tracking and disturbance rejection in the low frequency domain, to fulfill the performance requirements of the PFC function. In the two DOF architecture, this corresponds to penalizing the feedforward sensitivity $\boldsymbol{W}_{ref} - \boldsymbol{S}_o\boldsymbol{G}_{yu}\boldsymbol{K}_r$ for reference tracking, and the disturbance sensitivity $\boldsymbol{S}_o\boldsymbol{G}_{yd}$ for disturbance rejection. High weighting is applied to the error at low frequencies, with a first-order roll-off towards higher frequencies. This frequency-dependent weighting is imposed through $\boldsymbol{W}_e$. The crossover frequency $\omega_{0,e}$ is chosen in a suitable range of the rigid-body dynamics, here 7.5 rad/s. The resulting weighting function is shown as the black curve in Fig. 7a.

The static weight $\boldsymbol{V}_e$ scales the error signals and enables trade-offs when multiple error signals are considered. In the present design only the error in load factor or roll acceleration is included. The static weight is therefore chosen as unity, $\boldsymbol{V}_e = 1$, see Fig. 7a. The static input weights $\boldsymbol{V}_r$, $\boldsymbol{V}_d$, and $\boldsymbol{V}_n$ scale the reference, disturbance, and noise inputs relative to the tracking error. To ensure a steady-state gain of one for the tracked signals, the reference weight is selected as the inverse of the static error weight, $\boldsymbol{V}_r = \boldsymbol{V}_e^{-1}$. The gust disturbance weight is chosen as the inverse of the maximum singular value of the transfer function from gust disturbance to error (or tracked feedback), $\boldsymbol{V}_d = 1/\|\boldsymbol{G}_{yd}\|_\infty$. This choice ensures that the peak of the transfer function from disturbance to first exogenous output z_1 reaches 0 dB. The static noise weight is addressed in the section of the output weighting on $\boldsymbol{y}$. With respect to the error weight it is important that measurement noise does not dominate the transfer behavior to z_1, consequently the static weight must remain below unity. Figure 7b depicts the maximum singular values from reference, gust disturbance, and noise to first exogenous output, corresponding to the transfer functions of the generalized plant.

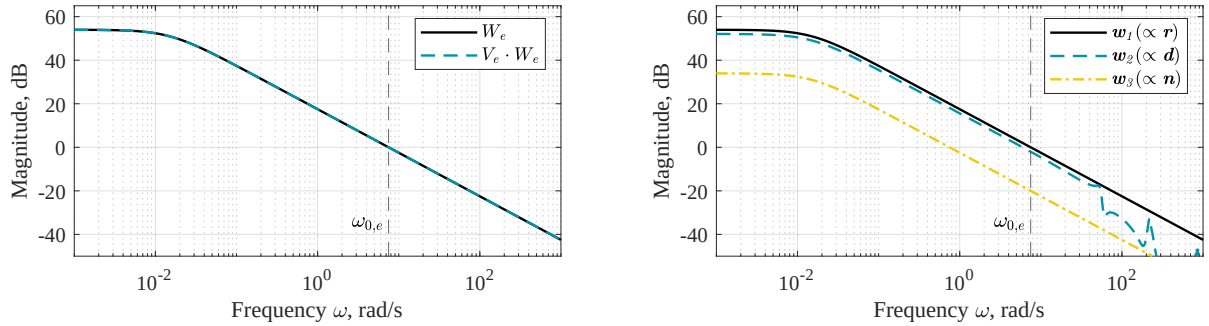

(a) Error weighting functions W_e and V_e. **(b) Weighted transfer function from $w_{1,2,3}$ to z_1.**

Fig. 7 Error weighting functions and resulting generalized plant transfer functions.

2. Performance Weighting Function

The performance channel targets aeroelastic performance in terms of gust load alleviation by exploiting the additional plant output $\boldsymbol{p}$, which is not used for feedback (see Eqs. 7 and 12). The performance load sensitivity $\boldsymbol{G}_{pd} - \boldsymbol{G}_{pu}\boldsymbol{K}_y\boldsymbol{S}_o\boldsymbol{G}_{yd}$ is penalized. The corresponding performance weighting function emphasizes the dominant peak in wing-root bending moment (WRBM) $M_{\mathrm{WR,x}}$ and wing-root torsion moment (WRTM) $M_{\mathrm{WR,y}}$, which the load alleviation aims to reduce. The peak is induced by the first flexible eigenmode, located at approximately $\omega_{f,1} = 55$ rad/s. The dynamic performance weight $\boldsymbol{W}_p$ introduces a second-order washout at frequencies below the first flexible mode, $\omega_{0,p1} < \omega_{f,1}$, and a second-order roll-off at frequencies above it, $\omega_{0,p1} > \omega_{f,1}$, thereby isolating the frequency band of this eigenmode. The magnitude level of this frequency band relative to the 0 dB line is determined by the static performance weight $\boldsymbol{V}_p$. It is chosen as the inverse of the $\mathcal{H}_\infty$-norm from exogenous disturbance $\boldsymbol{w}_2$ to performance output $\boldsymbol{p}$, and scaled by a tuning parameter p_p to lift the modal peak above the 0 dB line. Varying p_p enables a trade-off between the GLA objective and the remaining objectives. The resulting static performance weight is given by: $\boldsymbol{V}_p = p_p \cdot 1/\|\boldsymbol{G}_{pd}\boldsymbol{V}_d\|_\infty$. Figure 8a shows dynamic and static performance weight, while Fig. 8b illustrates their effect on the generalized plant transfer function from the gust disturbance input $\boldsymbol{w}_2$ to the performance output $\boldsymbol{z}_2$. The performance outputs contains the wing-root bending and torsion moment, with the torsion moment weighted at one quarter of the bending moment.

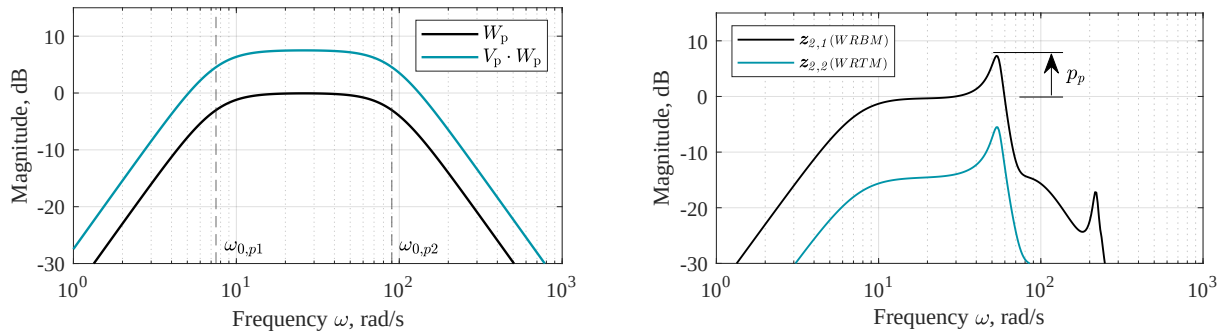

(a) Performance weighting functions W_p and V_p. **(b) Weighted transfer function from w_2 to z_2.**

Fig. 8 Performance weighting functions and resulting generalized plant transfer functions.

3. Control Activity Weighting Function

Control activity must be limited to avoid actuator commands that cannot be realized by the physical plant. This is accomplished by shaping the feedforward and feedback control sensitivities, $\boldsymbol{S}_i\boldsymbol{K}_r$ and $\boldsymbol{K}_y\boldsymbol{S}_o$, using the static and dynamic control weights $\boldsymbol{V}_u$ and $\boldsymbol{W}_u$. High-frequency control action is suppressed by the dynamic weight $\boldsymbol{W}_u$, which increases in magnitude above the cutoff frequency $\omega_{0,u}$, via a second-order function, as shown in Fig. 9a.

The static weight $\boldsymbol{V}_u$ limits control activity across all frequency ranges. Since hard actuator constraints cannot be enforced within the standard robust control framework, control limitations are imposed as soft constraints. The static

weight is selected such that the generalized plant transfer function exceeds the 0 dB line when the maximum allowable control surface deflection is violated for the largest commanded reference. With the reference weight normalized to unity, $\boldsymbol{V}_r = 1$, this results in a static control weight defined as: $\boldsymbol{V}_u = p_u \cdot r_{max}/u_{max}$, meaning it is tightened by the largest expected reference command, and multiplied by the inverse of the maximum admissible control surface deflection u_{max}. The parameter p_u can be used for tuning the relative penalty on control activity.

The roll-off frequency of the dynamic weight and the static scaling parameter p_u can be selected individually for each control surfaces, thereby enabling implicit control allocation. This design choice allows the assigned task and constraints of the individual actuators to be reflected in the controller synthesis. Based on comparisons with a representative full-scale aircraft configuration, the inner control surfaces (see Fig. 3) are treated as low-speed "flaperons", while the outer control surfaces are regarded as high-speed ailerons. Note that this difference in actuator rate capability is not present in the wind tunnel experiment. Following this distinction, the two inner control surfaces (1,2) are assigned exclusively to PFC tasks and therefore employ a low roll-off frequency, $\omega_{0,u1} = 10$ rad/s. The outer control surfaces (3,4) are used for both PFC and GLA tasks and therefore feature a higher roll-off frequency, $\omega_{0,u2} > \omega_{0,u1}$, selected to 60 rad/s. To preserve sufficient bandwidth for aeroelastic control, the static weight for the outer control surfaces is chosen slightly larger, reducing their contribution to low-frequency PFC tasks. The resulting weighting functions are shown in Fig. 9b, where the inner and outer control surfaces are depicted in black and blue, respectively.

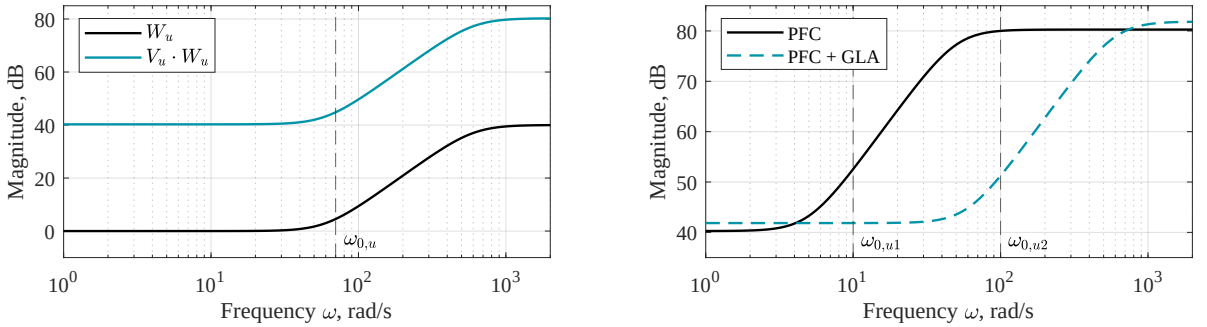

(a) Control activity weighting functions W_u and V_u. **(b) Individual weighting of the control surfaces.**

Fig. 9 Control activity weighting functions and individual control surface weighting.

4. Output Weighting Function

Multiple sensors are available for feedback, see Section II.C. Shaping the complementary sensitivity $\boldsymbol{T}_o$ from noise to plant output allows the relative contribution of the available sensors to be shaped over the frequency bandwidth while providing noise attenuation. Additionally, appropriate output weighting ensures nominal closed-loop stability. Note that robust stability and robust performance are treated in the subsequent Section IV.C. The complementary sensitivity is shaped through the combination of the output weights $\boldsymbol{V}_y$, $\boldsymbol{W}_y$ with the static noise weight $\boldsymbol{V}_n$.

The static noise weight is selected as a fraction of the static reference weight, $\boldsymbol{V}_r = 1$, to avoid conflict with the error channel used for reference tracking and disturbance rejection. Its magnitude is chosen based on the expected signal-to-noise ratios of the respective sensors or feedback variables. In the present design, noise levels of 20% are assumed for forces and moment measurements and a 10% for acceleration sensors, resulting in $\boldsymbol{V}_n = [0.2, 0.1, 0.1]$.

The static output weight is defined as the inverse of the static noise weight, allowing the complementary sensitivity function to be shaped without additional scaling. This weight is subsequently adjusted, if necessary, to achieve satisfactory disk-based stability margins [38] for the nominal system. In the nominal case, stability margins can be directly related to the peak values of the sensitivity and complementary sensitivity function [13, 17, 37], with a 6 dB gain margin corresponding to a sensitivity peak not exceeding two. In μ-synthesis however, the desired loop shapes are imposed on the system including uncertainty, and such explicit criteria cannot be directly imposed. Instead, a tuning parameter p_y is initialized to unity and increased if nominal stability proves insufficient. The resulting static output weight is therefore given by: $\boldsymbol{V}_y = p_y \cdot \boldsymbol{V}_n^{-1}$.

The dynamic output weight $\boldsymbol{W}_y$ constrains sensor utilization across different frequency ranges. In the low-frequency regime, the controller is intended to rely primarily on balance feedback, emulating sensors located within the aircraft fuselage. The acceleration sensors on the wing exhibit unfavorable noise characteristic in this range, which may induce

low-frequency oscillations, and their contribution is therefore attenuated. This is achieved by imposing a high output weight at low frequencies that rolls off toward higher frequencies, where the GLA function relies predominantly on wing acceleration measurements. The resulting weighting function is shown in Fig. 10b, with a cutoff frequency of $\omega_{0,\mathrm{y,y}} = 5$ rad/s. At high frequencies, the contribution of the balance measurements is reduced, as corresponding sensors located in the fuselage of a full-scale aircraft do not adequately capture the flexible deformation of the wing. A high output weight is imposed with a cutoff frequency of $\omega_{0,\mathrm{y,r}} = 45$ rad/s, as shown in Fig. 10b.

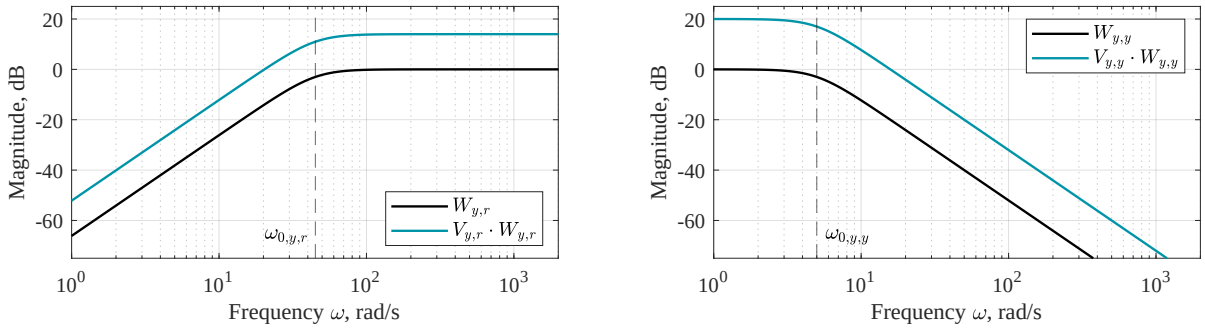

(a) Tracked feedback variables. **(b) Additional feedback variables.**

Fig. 10 Output weighting functions for tracked and additional feedback variables.

C. Uncertainty Modeling for Robustness Objectives

In μ-synthesis, robustness is addressed by introducing uncertainties $\boldsymbol{\Delta}$ to form the uncertain plant $\tilde{\boldsymbol{G}}$, as indicated in Figs. 5 and 6. When the synthesis optimizes robust performance, the loop shaping objectives (Section IV.B) are enforced not only for the nominal plant, but for the entire set of possible plants, thereby targeting worst-case performance under the modeled uncertainties. These can be assigned to individual plant parameters, enabling a detailed uncertainty modeling. However, the available plant model from Eq. 7 includes not only aerodynamic coefficients, as commonly used for PFC, but a detailed aerodynamic distribution, making such fine-grained uncertainty modeling complex. Instead, uncertainties are introduced at the plant inputs and outputs, i.e. actuators and sensors, to ensure adequate robustness. Uncertainty is introduced in the form of structured, multiplicative uncertainty [13, 14], expressed as:

$$\tilde{\boldsymbol{G}} = (\boldsymbol{I} + \boldsymbol{W}_o \boldsymbol{\Delta}_o) \cdot \boldsymbol{G} \cdot (\boldsymbol{I} + \boldsymbol{W}_i \boldsymbol{\Delta}_i), \qquad \boldsymbol{\Delta}_{i/o} = \mathrm{diag}(\delta_{i/o,m}),\ \|\boldsymbol{\Delta}_{i/o}\|_\infty < 1, \tag{14}$$

where $\boldsymbol{\Delta}_{i/o}$ represents the matrix of structured uncertainty at the inputs or outputs, with complex uncertainty elements δ_m, and $\boldsymbol{W}_i$ and $\boldsymbol{W}_o$ are the corresponding input and output uncertainty weighting function. The nominal plant is denoted $\boldsymbol{G}$, see Eq. 7. The block diagram representation of Eq. 14 is shown as the generalized plant from Fig. 6.

Structured uncertainty implies that $\boldsymbol{\Delta}_i$, $\boldsymbol{\Delta}_o$ are diagonal, meaning the uncertainty of individual actuators or sensors are independent and do not interact with each other. This prevents nonphysical interactions, which would otherwise lead to overly conservative robustness requirements. The uncertainties are complex, capturing deviations in both magnitude and phase. While not directly physical, this can be interpreted as representing uncertainty in gain and time delay. Using complex uncertainties is also numerically advantageous, as it permits the formulation of the μ-synthesis problem using only D-scales rather than both D- and G-scales [16, 39].

The uncertainty weighting functions for the actuators (plant inputs), balance measurements, and acceleration sensors (plant outputs) are selected based on physical insight [40], with the resulting functions displayed in Fig. 11. The actuators are modeled with a low-frequency uncertainty of 10% (-20 dB), increasing to 20% (-14 dB) at high frequencies. This transition occurs at half the actuator cutoff frequency, $\omega_{0,\mathrm{act}}$, see Table 1. Figure 11a shows the resulting weighting function. Acceleration sensors follow a similar shape, with uncertainties of 5% (-26 dB) at low frequencies and 10% (-20 dB) at high frequencies. Since no sensor cutoff frequency is identified in the model, the crossover is set at 90 rad/s. The balance exhibits the same low-frequency uncertainty as the accelerometers but rises to 50% (-6 dB), with a crossover at 20 rad/s. This higher uncertainty reflects the increased modeling uncertainty of balance measurements, as the representative sensors would be located at different locations on a full-scale aircraft. The resulting transfer functions are shown in Fig. 11b.

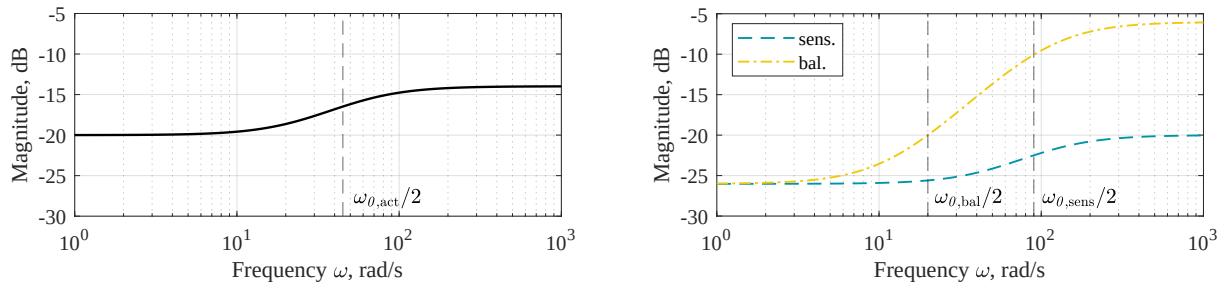

(a) Uncertainty on actuators, W_i. **(b) Uncertainty on senors and balance, W_o.**

Fig. 11 Uncertainty weight on actuators (plant input) and acceleration sensors, balance (plant output).

D. Synthesis and Numerical Evaluation

Both controllers are designed using μ-synthesis. The generalized plant shown in Fig. 6 is augmented with the weighting functions and uncertainty descriptions defined in Sections IV.B and IV.C, respectively. This generalized plant can be reformulated into the standard interconnection structure, as shown on the left in Fig. 12. Local uncertainties are collected and isolated into the $\boldsymbol{\Delta}$-block, yielding a top-level diagonally-structured uncertainty. The exogenous inputs $\boldsymbol{w}$ and outputs $\boldsymbol{z}$ are defined as in Eq. 13. Interconnection with the controller $\boldsymbol{K}$ yields the uncertain closed-loop system $\boldsymbol{N}(\boldsymbol{P},\boldsymbol{K})$, as depicted on the right in Fig. 12. The μ-synthesis procedure seeks to achieve robust performance by minimizing the $\mathcal{H}_\infty$-norm from $\boldsymbol{w}$ to $\boldsymbol{z}$ of the closed-loop system $\boldsymbol{N}$ under worst-case uncertainty $\boldsymbol{\Delta}_{wc}$, which itself depends on the controller $\boldsymbol{K}$. Therefore, μ-synthesis iterates between optimization of the controller using $\mathcal{H}_\infty$-synthesis and robustness analysis using μ. Details on the underlying algorithm are provided in [13–15]. The approach is implemented in software such as MATLAB [41] and can be readily applied.

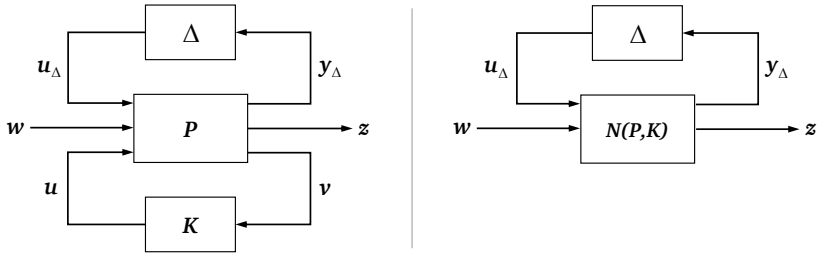

Fig. 12 Standard interconnection structure (left) and uncertain closed-loop (right).

The synthesis results are analyzed numerically in the frequency domain, before the wind tunnel results are presented the the following Section V. Frequency domain results are very similar for both designed controllers, which is why only the results of the controller for load factor tracking combined with load alleviation are presented. Experimental results for both controllers are shown in the following section. Figure 13a evaluates PFC performance by presenting the maximum singular values of the closed-loop system from the reference to the tracked feedback output, the error, and the control command. The underlying transfer functions are given in Eq. 12. Figure 13b evaluates GLA performance in terms of maximum singular values between gust disturbance and performance variables, for open and closed-loop.

Figure 13a demonstrates satisfactory tracking behavior in the low frequency range, up to the target bandwidth of 5 rad/s, as specified by the reference filter (roll-off frequency $\omega_{0,r}$) and the error weight. The transfer function from the reference to the tracked variable reaches 0 dB, indicating accurate tracking. Effective disturbance rejection is observed over the same bandwidth, as reflected by the response from reference to error. Control action remains adequately limited (as seen in the time-domain signals from the experiment presented further below), and the controller gain exhibits a roll-off toward high frequencies. Figure 13b confirms that in addition to the PFC tasks the controller also achieved the desired GLA performance. The first peak in loads associated with the first flexible eigenmode is significantly reduced. A slight exceedance of the open-loop gain is observed at lower frequencies, caused by the imposed control activity weighting on the inner control surfaces. At higher frequencies the open-loop gain is never exceeded, indicating that no secondary modes are excited by the closed-loop system.

Stability and robustness are assessed by means of a μ-analysis, the result of which are shown in Fig. 14. As discussed previously, the synthesis targets robust performance, represented by the black curve. In addition, the SSV μ provides

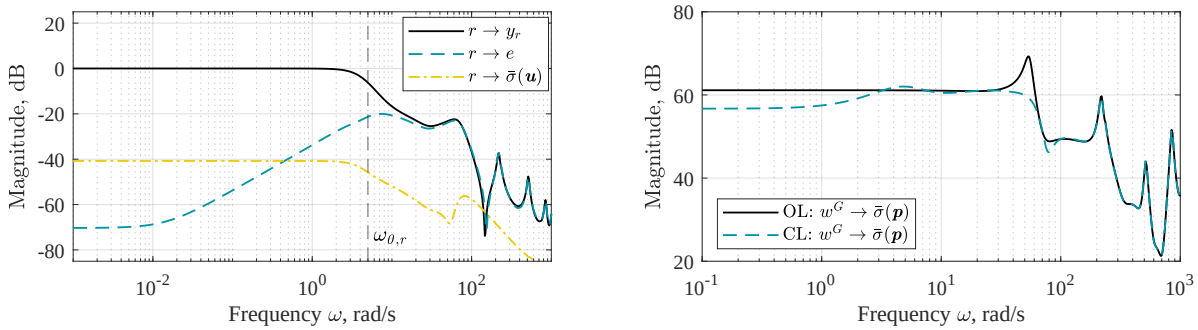

(a) Reference to feedback, error, and command output. **(b) Gust to performance output, open and closed-loop.**

Fig. 13 Frequency domain evaluation of the closed-loop system.

measure of nominal performance and robust stability, shown by the blue and yellow curves, respectively. Robust stability indicates whether the closed-loop system remains stable under the defined uncertainties. The corresponding SSV is the reciprocal of the maximum singular value $\bar{\sigma}(\boldsymbol{\Delta})$ of the smallest uncertainty matrix $\boldsymbol{\Delta}$ that renders the closed-loop system singular. For the integrated control design, the value remains below 0.3 for all frequencies, implying that the worst-case uncertainty could be increased by at least a factor of 3.3 before instability occurs. Nominal performance is also satisfied, with the peak value of the corresponding SSV just reaching unity. This indicates that in absence of uncertainty, all performance requirements imposed by the weighting functions are met, i.e. an $\mathcal{H}_\infty$-norm of one is achieved for the nominal closed-loop system. Robust performance exceeds unity, with a peak value of 1.53. This indicates a performance degradation of approximately 50% under worst-case uncertainty. Given the demanding performance specifications, this degradation is deemed acceptable. Moreover, the robust performance μ-curve is relatively flat across frequency, suggesting a well-balanced design in which no single objective dominates or limits the reduction of μ.

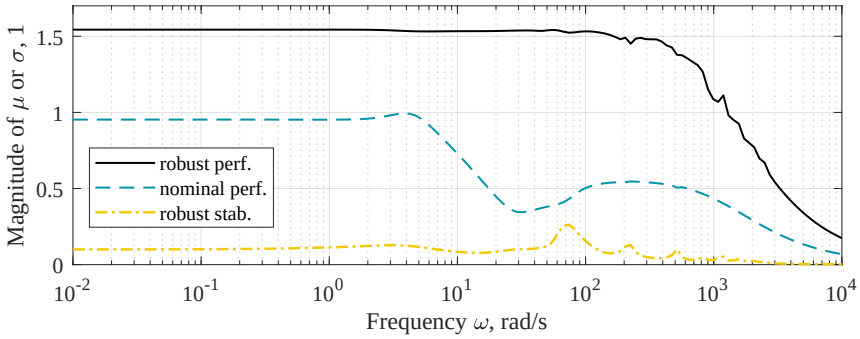

Fig. 14 Results of the μ-analysis for the integrated controller.

Finally, nominal stability is additionally assessed using disk-based stability margins, summarized in Table 3. For the multiloop case, the results are consistent with the results for robust stability, as the peak SSV is directly related to the achieved margins. Multiloop disk-based gain margins slightly exceeding 7 dB are obtained at both the input and output, while the multiloop disk-based phase margin exceeds the desired 40°. The loop-at-a-time margins are larger in both gain and phase, at the cost of being less conservative. Overall, the integrated controller exhibits excellent stability and robustness properties. The controller performance is further analyzed in the following section on wind tunnel results.

Table 3 Disk-based stability margins for the integrated controller.

Margin type	Cut point	Gain margin	Phase margin	Frequency	Worst loop
multiloop	input	2.5 (8.1 dB)	47.0°	78.6 Hz	-
multiloop	output	2.4 (7.6 dB)	45.0°	75.5 Hz	-
loop-at-a-time	input	4.3 (12.7 dB)	63.8°	82.0 Hz	flap 5
loop-at-a-time	output	4.2 (12.4 dB)	63.2°	81.7 Hz	sensor 5b

V. Experimental Evaluation in the Wind Tunnel

Both integrated controllers are evaluated experimentally in the wind tunnel setup shown in Fig. 15. The flexible wing is clamped at the root to a wind tunnel balance, enabling measurement of the resulting forces and moments. The wing is instrumented with acceleration sensors and trailing-edge control surfaces, as introduced in Section II.C and illustrated in Fig. 3. The model angle-of-attack can be adjusted, however it is fixed at 0° for the present experiment. A gust generator installed upstream produces continuous (sine-like) or discrete (1-cosine-like) gust disturbances in the flow. Aerodynamic and gust conditions are monitored using a five whole probe mounted on the wind tunnel ceiling. Further details on the experimental setup are provided in [42], additional information on the flexible wing in [43] and on the gust generator in [44].

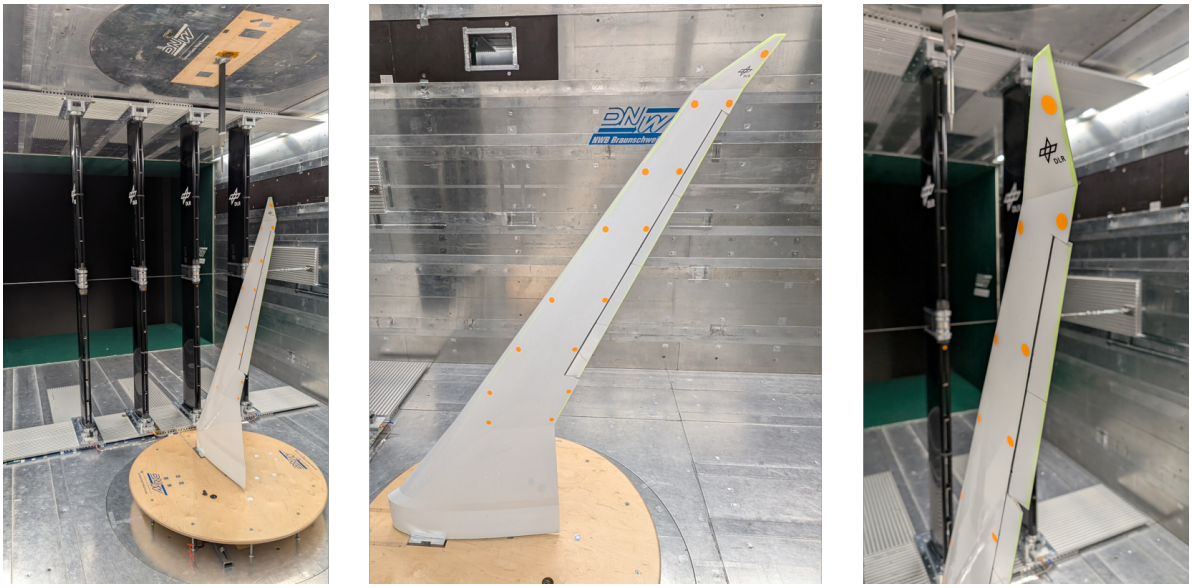

Fig. 15 Experimental setup of the wind tunnel test, with gust generator and flexible wing.

The experiments are conducted at a freestream velocity of 30 m/s under atmospheric conditions. The controllers are implemented on a real-time control system operating at a sample frequency of 1000 Hz. Sensor signals from the balance and acceleration measurements are processed by the controller, which generates control commands that are converted into duty cycles and applied to the electromechanical actuators operating at 560 Hz. All measurements are recorded using a data acquisition system with a sampling rate of 10 kHz. In the following, the experimental results obtained with both integrated controllers are presented.

A. Wind Tunnel Evaluation: Reference Tracking

The reference tracking capability of the integrated controllers is evaluated to assess performance with respect to the primary flight control task. Step inputs, harmonic signals, and arbitrarily varying reference commands are applied, and the corresponding system responses are analyzed. For these tests, the gust generator is switched off, nevertheless residual aerodynamic disturbances continue to excite the wing.

1. Integrated Load Factor and GLA Controller

Load factor n_z tracking is emulated by a tracking the vertical force measured at the wind tunnel balance, $F_{\text{bal,z}}$, as described in Section III. Figure 16 presents the evaluation of representative load factor tracking for step reference commands. As shown in Fig. 16a, these step inputs (black dashed line) are transformed into a smooth ideal reference signal (yellow line) with dynamics defined by the reference filter, see Section IV. This ideal reference is closely tracked by the closed-loop system, as indicated by the measured response (blue line). The results demonstrate satisfactory tracking performance. The deviation between the step input and the ideal reference is expected. While a faster rise time could be achieved by selecting faster reference dynamics, this would require increased control activity and introduce a performance trade-off with the load alleviation function due to physical limitations in shaping the sensitivity functions [45].

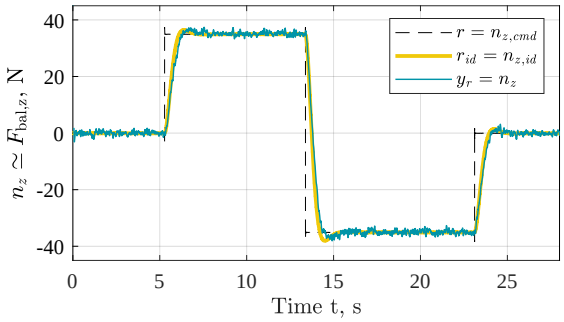

(a) Tracking of load factor / vertical force.

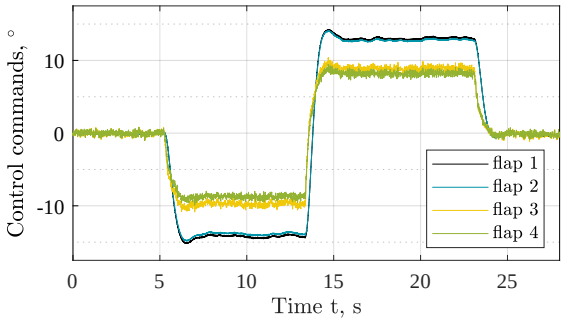

(b) Commanded control surface deflection.

Fig. 16 Evaluation of load factor reference tracking using step commands.

The control commands corresponding to the step reference tracking are shown in Fig. 16b. As discussed when introducing the control functions (Section III), load factor tracking is achieved through direct lift control. Changes in lift, and consequently in load factor, are realized via the trailing-edge control surfaces on the wing, enabling a fast response. Positive flap deflection (downwards) generates a negative vertical force (upwards, lift) and a negative load factor. It can be seen that the inner flaps (1 and 2) are deflected more than the outer flaps (3 and 4). This behavior is intentional and incorporated in the controller design, as detailed in Section IV, and illustrated in Fig. 9b. The inner flaps contribute solely to the reference tracking task (PFC), while the outer flaps also perform GLA functions, necessitating sufficient bandwidth to accommodate both objectives. In all cases, the flap deflections remain within the limit of 15°, respecting the soft constraints imposed by the control activity weighting.

2. Integrated Roll and GLA Controller

The second controller emulates roll acceleration $\dot{p}$ tracking through roll moment $M_{\mathrm{bal,x}}$ tracking, using the measured moment from the wind tunnel balance. This controller also achieves satisfactory tracking performance, as depicted in Fig. 17a. The applied reference command (black dashed line) is converted into a smooth ideal reference signal (yellow line), which is closely followed by the measured system response (blue line). Unlike the previous case, the reference inputs are not pure steps, they consist of a variable signal with an initial step up and down followed by a smoother trajectory. For all inputs, the closed-loop system tracks the ideal reference accurately. The observed time lag between the commanded reference and the ideal reference is attributed to the dynamics of the reference filter, as discussed above. This lag becomes more pronounced when a harmonic motion is applied, as in the second part of the presented response.

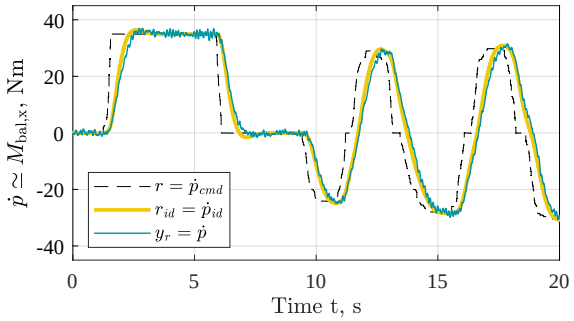

(a) Tracking of roll acceleration / roll moment.

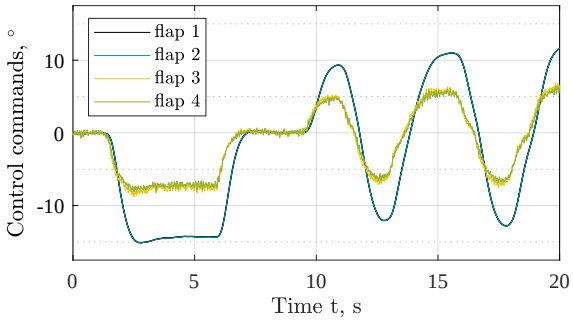

(b) Commanded control surface deflection.

Fig. 17 Evaluation of roll reference tracking using variable commands.

The associated control commands are shown in Fig. 17b. Following the coordinate definition introduced in Fig. 3, a positive roll acceleration or moment is defined with decreasing lift, meaning the control surfaces deflect negatively (upwards). Similar to the load factor tracking case, the inner flaps are used roughly twice as much as the outer flaps to generate the required roll maneuver. This allocation sparing perseveres bandwidth on the outer flaps, allowing them to simultaneously suppress gust loads.

B. Wind Tunnel Evaluation: Gust Load Alleviation

After evaluating reference tracking, the gust load alleviation capabilities are assessed. Both integrated controllers exhibit comparable performance for this aeroelastic objective, therefore only the results obtained with the roll tracking controller are presented. For this evaluation, the reference command is set to zero, while the gust generator introduces a continuous, sine-like gust disturbance into the airflow. The primary performance metric is the WRBM $M_{\text{bal,x}}$, defined with respect to the loads reference axis (LRA), see Fig. 3. Since this quantity is not directly measurable, it is reconstructed from the forces and moments measured by the wind tunnel balance, mapped to the location and orientation of the LRA. Figure 18 presents the resulting WRBM response for a continuous gust at 8.75 Hz or 55 rad/s, which is close to the first eigenfrequency of the flexible wing at a freestream velocity of 30 m/s (compare to Fig. 4). This operating point leads to the highest load amplitudes and therefore shows the highest effectiveness of the aeroelastic controller. In the time sequence presented, the integrated controller is initially inactive, while the gust excites the wing. At time t = 12.5 s, the controller is enabled, beginning to reduce the loads observed on the wing.

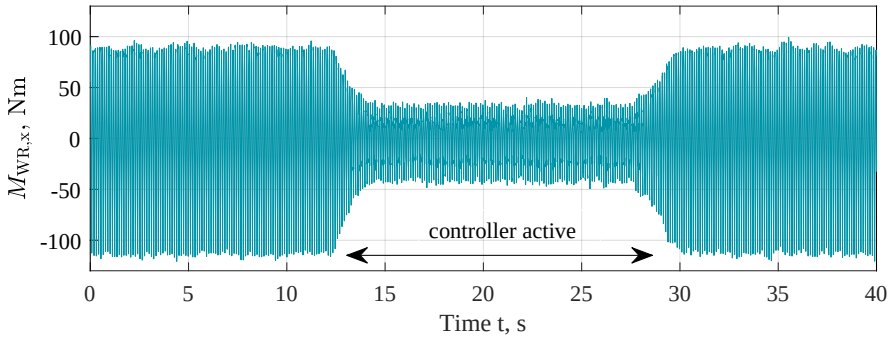

Fig. 18 Wing-root bending moment during a continuous gust excitation with 8.75 Hz.

The root mean square (RMS) of the bending moment is reduced by approximately 45 Nm, corresponding to a relative reduction of about 66%. A zoomed-in view of the bending moment response is displayed in Fig. 19a, where the cases with and without active control are superimposed. The asymmetry observed in the WRBM response originates from the gust generator, which produces stronger updrafts (negative moments) than downdraft. The associated wing-root torsion moment is likewise attenuated, although it is not shown here.

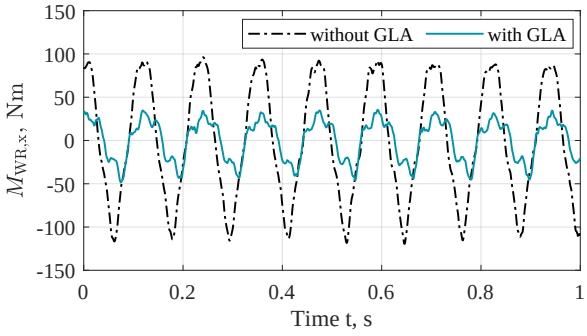

(a) Wing-root bending moment, with and without GLA.

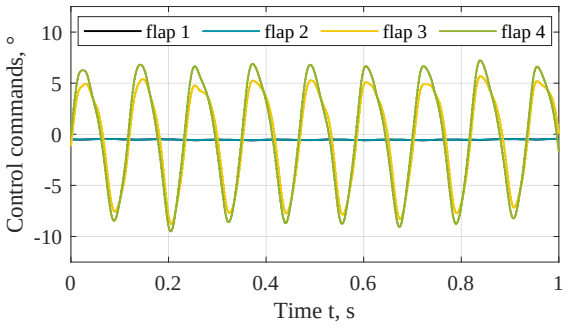

(b) Flap commands during GLA.

Fig. 19 Loads and flap commands during gust load alleviation on a 8.75 Hz continuous gust.

The control activity to achieve this load reduction is shown in Fig. 19b. As intended, only the two outer flaps are engaged to increase the damping of the first aeroelastic mode, while the inner control surfaces remain at their neutral position. This control allocation strategy was discussed in Section IV.B. Flap 3 and 4 are exhibit comparable deflection amplitudes, reaching a maximum of approximately 8°. Since the 8.75 Hz excitation represents the worst-case gust scenario, the control surface deflection limits can be considered satisfied. The frequency domain results in Fig. 13b indicate gust load reduction over the entire frequency range of interest. This behavior is also confirmed experimentally, although the results are omitted here for brevity.

C. Wind Tunnel Evaluation: Combined Controller with Tracking and Load Alleviation

Finally, the integrated controller is evaluated under simultaneous reference tracking and gust load alleviation. During this test, various reference commands are applied while the gust generator is alternately activated and deactivated, thereby emulating gust encounters during maneuvering. This allows the analysis of controller performance and the distribution of control bandwidth under the combined tasks.

1. Integrated Load Factor and GLA Controller

Combined load factor tracking and gust load alleviation are presented in Figs. 20 and 21. The controller operates continuously and receives step commands as reference inputs, while the flexible wing is intermittently subjected to gust encounters. These encounters, periods during which the gust generator imposes a harmonic gust of 8.75 Hz, are indicated as *GG active* in the plots. Figure 20a illustrates that the integrated controller maintains the desired load factor or vertical force during gust excitation: although the measurement is superimposed by gust-induced fluctuations, its mean value matches the reference. At the same time, the reduction in WRBM is visible in Fig. 20b, where results obtained without active GLA are overlaid for comparison. The achieved load alleviation performance is similar to that shown in Fig. 18.

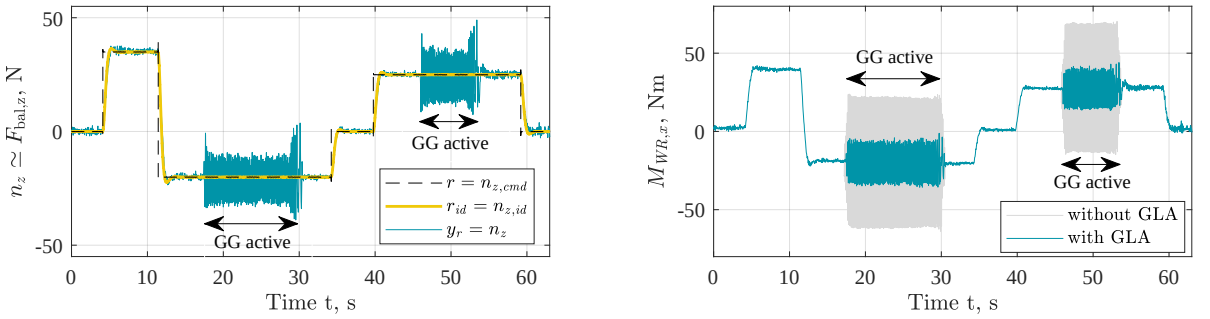

(a) Load factor / vertical force. **(b) Wing-root bending moment.**

Fig. 20 Evaluation of load factor tracking combined with gust load alleviation.

The associated control surface commands are shown on the left in Fig. 21, with an enlarged view of a time excerpt provided on the right. During gust encounters, the inner flaps remain at their static deflection required to generate the commanded load factor or vertical force. In contrast, the outer flaps deflect about this static position to alleviate gust-induced loads, as visible in the enlarged view. Once the gust excitation ceases, all control surfaces return to their static deflection position. It should be noted that the activation or deactivation of the gust generator introduces additional disturbances, to which the control surfaces respond. The results demonstrate that for the combined case of a 35 N vertical force demand and a worst-case gust excitation of 8.75 Hz, all control surface deflection remain within the allowable limit of ±15°.

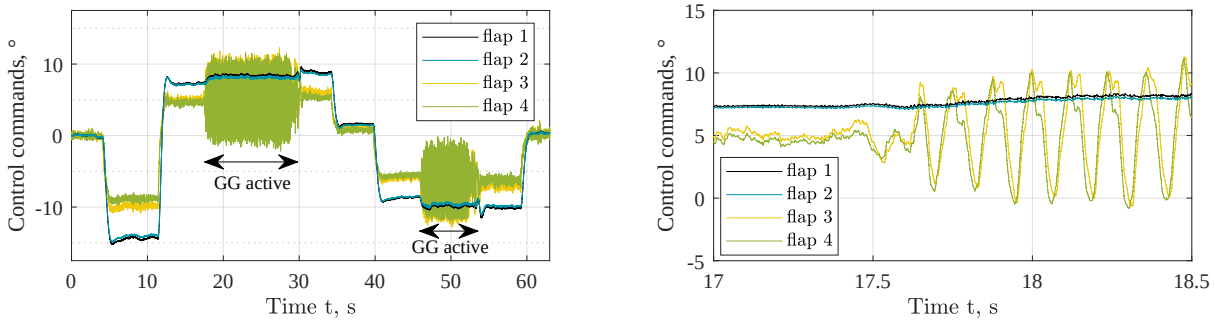

Fig. 21 Commanded control surface deflection during load factor tracking combined with GLA.

2. Integrated Roll and GLA Controller

Similar results are achieved for the second controller, which combines roll acceleration (or roll moment) tracking with gust load alleviation. Figure 22a shows the applied reference commands and the corresponding tracked feedback variable, while Fig. 22b depicts the associated control surface deflections. The results indicate that reference tracking performance is not adversely affected by simultaneous gust encounters. To follow the reference, the (outer) control surfaces adjust their static deflection while superimposing oscillatory motions to mitigate gust-induced loads. This demonstrates the effectiveness of the integrated control design approach.

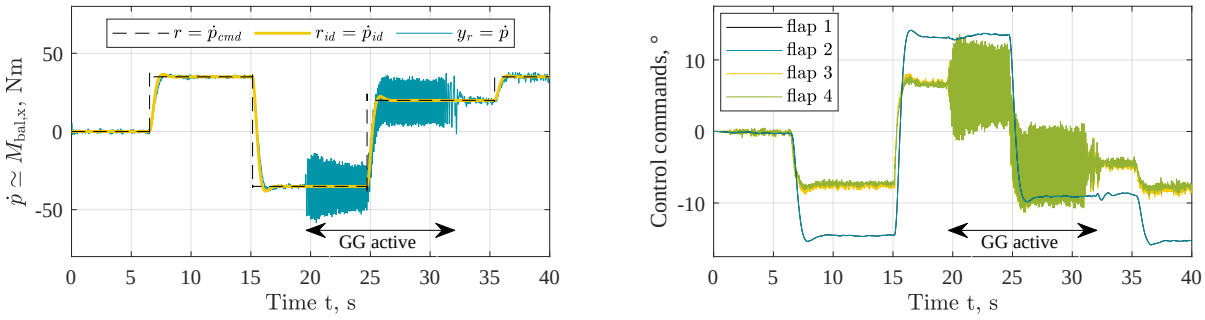

(a) Roll acceleration / roll moment.

(b) Commanded control surface deflection.

Fig. 22 Evaluation of roll command tracking combined with gust load alleviation.

VI. Conclusion and Outlook

This paper presented a design methodology for integrated primary flight and aeroelastic control. Using μ-synthesis robust control, a unified controller was developed that simultaneously tracks reference commands and alleviates gust-induced loads. By detailing the control architecture, the formulation of the generalized plant, the selection of weighting functions, and the incorporation of uncertainties, the work provides a guideline for designing controllers for similar integrated applications. The use of μ-synthesis proved advantageous, as it enables optimization of closed-loop performance not only for the nominal plant, but over the entire set of plants defined by the modeled uncertainty.

The methodology was demonstrated on two representative control tasks: load factor tracking combined with gust load alleviation in the longitudinal axis, and roll rate tracking combined with gust load alleviation in the lateral axis. The resulting controllers were validated experimentally in a wind tunnel test using a flexible wing model. Since the setup does not permit rigid-body motion, the primary flight control tasks were reformulated into experimentally realizable representative tasks. This demonstrates the applicability of wind tunnel experiments to validate not only aeroelastic control functions, but also primary flight control concepts. The test results demonstrated a successful integration of classical primary flight control tasks, stability and command augmentation, with gust disturbance rejection.

Future work will focus on integrating the developed inner loop controllers into a complete primary flight control framework. In particular, embedding these within a nonlinear dynamic inversion architecture is envisioned, where they would act as error controllers while continuing to provide gust load alleviation. Numerical validation using a full-aircraft simulation is planned to assess the interactions between the integrated controller, the outer loops, and the aircraft dynamics. To further enhance the validation of primary flight control functions, future wind tunnel testing should extend beyond isolated wing models. Testing controllers on a half-model configuration that combines wing, fuselage, and empennage, would enable the inclusion of elevator control surfaces and simulated pitch and heave dynamics. Such a setup would significantly increase validation capabilities and facilitate the investigation of more advanced integrated control functions.

Acknowledgments

This work was conducted within the *Sensor and AI Fusion for Enhanced PeRformance and Reliability (SAFER^2)* project of the German Aerospace Center (DLR). The authors would like to thank all contributors involved in planning, preparation and execution of the wind tunnel experiment, making the integrated control test possible. Special thanks to Charlotte Hanke, Thomas G. Schmidt, Anna Altkukatz, Lukas Koida, Marc Braune, and Holger Mai (test execution, gust generator design, measurement technology and data acquisition), Johannes Dillinger (wind tunnel model development and finite element modeling), Robin Volkmar, Keith Soal, and Marc Böswald (structural identification of the model), Simon Schulz, Ramesh Konatala, and Thiemo Kier (support during modeling and controller testing), and the wind tunnel team of the DNW-NWB.

References

[1] Binder, S., Wildschek, A., and De Breuker, R., "The Interaction Between Active Aeroelastic Control and Structural Tailoring in Aeroservoelastic Wing Design," *Aerospace Science and Technology*, Vol. 110, 2021. https://doi.org/10.1016/j.ast.2021.106516.

[2] Krengel, M. D., "Load Alleviation and Wing Planform Optimization for Fuel Efficient Conceptual Aircraft Design," PhD thesis, Technical University Braunschweig, Braunschweig, Germany, 2025. https://doi.org/10.57676/0ae9-hz13.

[3] Regan, C. D., and Jutte, C. V., "Survey of Applications of Active Control Technology for Gust Alleviation and New Challenges for Lighter-Weight Aircraft," Technical Report, TM-2012-216008, NASA, 2012. URL https://ntrs.nasa.gov/citations/20120013450.

[4] Chin, J., "Universal-type gust alleviation system for aircraft," U.S. Patent 4905934. Grumman Aerospace Corporation., 1990. https://www.freepatentsonline.com/4905934.html.

[5] Ramsey, H., and Lewolt, J., "Design Maneuver Loads for an Airplane with an Active Control System," *20th Structures, Structural Dynamics, and Materials Conference*, AIAA, St. Louis, USA, 1979, pp. 456–463. https://doi.org/10.2514/6.1979-738.

[6] Stevens, B. L., Lewis, F. L., and Johnson, E. N., *Aircraft Control and Simulation*, 3rd ed., John Wiley & Sons, 2016.

[7] Schmidt, D. K., *Modern Flight Dynamics*, 1st ed., McGraw-Hill, 2012.

[8] Looye, G., and Joos, H.-D., "Design of Autoland Controller Functions with Multiobjective Optimization," *Journal of Guidance, Control, and Dynamics*, Vol. 29, No. 2, 2006, pp. 475–484. https://doi.org/10.2514/1.8797.

[9] König, K., and Schuler, J., "Integral Control of Large Flexible Aircraft," *RTO Meeting Proceedings 36, Structural Aspects of Flexible Aircraft Control*, Research and Technology Organization (RTO) of NATO, Ottawa, Canada, 1994. URL https://apps.dtic.mil/sti/citations/ADA388195.

[10] Kubica, F., and Livet, T., "Flight Control Law Synthesis for a Flexible Aircraft," *AIAA Guidance, Navigation, and Control Conference*, AIAA, Scottsdale, USA, 1994. https://doi.org/10.2514/6.1994-3630.

[11] Hanel, M., "Integrated Flight and Aeroelastic Contorl of a Flexible Transport Aircraft," *AIAA Guidance, Navigation, and Control Conference and Exhibit*, AIAA, Boston, USA, 2019. https://doi.org/10.2514/6.1998-4297.

[12] Theis, J., Pfifer, H., Balas, G., and Werner, H., "Integrated Flight Control Design for a Large Flexible Aircraft," *American Control Conference (ACC)*, 2015. https://doi.org/10.1109/ACC.2015.7171927.

[13] Skogestad, S., and Postlethwaite, I., *Multivariable Feedback Control*, 2nd ed., John Wiley & Sons, Chichester, UK, 2005.

[14] Zhou, K., Doyle, J. C., and Glover, K., *Robust and Optimal Control*, 1st ed., Prentice Hall, 1995.

[15] Doyle, J. C., "Structured Uncertainty in Control System Design," *24th IEEE Conference on Decision and Control*, Fort Lauderdale, USA, 1985, pp. 260–265. https://doi.org/10.1109/CDC.1985.268842.

[16] Young, P. M., "Controller Design with Mixed Uncertainties," *Proceedings of the 1994 American Control Conference - ACC*, Vol. 2, Fort Lauderdale, USA, 1994, pp. 2333–2337. https://doi.org/10.1109/ACC.1994.752496.

[17] Stein, G., and Doyle, J. C., "Beyond Singular Values and Loop Shapes," *Journal of Guidance*, Vol. 14, No. 1, 1991. https://doi.org/10.2514/3.20598.

[18] Waszak, M. R., and Schmidt, D. K., "Flight Dynamics of Aeroelastic Vehicles," *Journal of Aircraft*, Vol. 25, No. 6, 1688, pp. 563–571. https://doi.org/10.2514/3.45623.

[19] Reschke, C., "Integrated Flight Loads Modelling and Analysis for Flexible Transport Aircraft," Ph.D. thesis, University of Stuttgart, Stuttgart, Germany, 2006. https://doi.org/10.18419/opus-3733.

[20] Hofstee, J., Kier, T., Cerulli, C., and Looye, G., "A Variable, Fully Flexible Dynamic Response Tool for Special Investigations (VarLoads)," *International Forum on Aeroelasticity and Structural Dynamics (IFASD)*, Amsterdam, Netherlands, 2003.

[21] Kier, T. M., and Hofstee, J., "VarLoads - eine Simulationsumgebung zur Lastenberechnung eines voll flexiblen, freifliegenden Flugzeugs," *Deutscher Luft- und Raumfahrtkongress (DLRK)*, DGLR, Dresden, Germany, 2004.

[22] Kier, T., and Looye, G., "Unifying Manoeuvre and Gust Loads Analysis Models," *International Forum on Aeroelasticity and Structural Dynamics (IFASD)*, Seattle, USA, 2009. URL https://elib.dlr.de/97798/.

[23] Bisplinghoff, R. L., Ashley, H., and Halfman, R. L., *Aeroelasticity*, 2nd ed., Dover Publications Inc., Mineola, USA, 1983.

[24] Wright, J. R., and Cooper, J. E., *Introduction to Aircraft Aeroelasticity and Loads*, 2nd ed., Wiley, Chichester, UK, 2015. https://doi.org/10.1002/9781118700440.

[25] Géradin, M., and Rixen, D. J., *Mechanical Vibrations*, 3rd ed., Wiley, 2015.

[26] Rao, S. S., *The finite element method in engineering*, 4th ed., Butterworth-Heinemann, 2005. https://doi.org/10.1016/B978-0-7506-7828-5.X5000-8.

[27] Albano, E., and Rodden, W. P., "A Doublet-Lattice Method for Calculating Lift Distributions on Oscillating Surfaces in Subsonic Flows," *AIAA Journal*, Vol. 7, No. 2, 1969. https://doi.org/10.2514/3.5086.

[28] Blair, M., "A Compilation of the Mathematics Leading to the Doublet Lattice Method," Technical Report, ADA256304, Air Force Wright Laboratory, 1992. URL https://apps.dtic.mil/sti/citations/ADA256304.

[29] Fielding, C., and Flux, P. K., "Non-linearities in Flight Control Systems," *The Aeronautical Journal*, Vol. 107, 2003. https://doi.org/10.1017/S0001924000013543.

[30] Tang, M., Böswald, M., Govers, Y., and Pusch, M., "Identification and Assessment of a Nonlinear Dynamic Actuator Model for Controlling an Experimental Flexible Wing," *CEAS Aeronautical Journal*, Vol. 12, 2021. https://doi.org/10.1007/s13272-021-00504-y.

[31] European Union Aviation Safety Agency, *Certification Specification and Acceptable Means of Compliance for Large Aeroplanes (CS-25)*, Amendment 27, 2023. URL https://www.easa.europa.eu/en/certification-specifications/cs-25-large-aeroplanes.

[32] Stalla, F., Looye, G., Kier, T. M., Michel, K., Ritter, M., Schmidt, T. G., Dillinger, J., and Tang, M., "Wind Tunnel Testing Active Gust Load Alleviation on an Experimental Wing," *International Forum on Aeroelasticity and Structural Dynamics (IFASD) 2024*, Den Haag, Netherlands, 2024. URL https://elib.dlr.de/205523/.

[33] Brockhaus, R., Alles, W., and Luckner, R., *Flugregelung*, 3rd ed., Springer, 2019. https://doi.org/10.1007/978-3-642-01443-7.

[34] Doyle, J., "Analysis of Feedback Systems with Structured Uncertainties," *IEE Proceedings, Pt. D, Control Theory and Applications*, Vol. 129, No. 6, 1982. https://doi.org/10.1049/ip-d.1982.0053.

[35] Doyle, J. C., Glover, K., Khargonekar, P. P., and Francis, B. A., "State-Space Solutions to Standard H_2 and H_∞ Control Problems," *IEEE Transactions on Automatic Control*, Vol. 34, No. 8, 1989. https://doi.org/10.1109/9.29425.

[36] Young, P. M., Newlin, M. P., and Doyle, J. C., "Practical Computation of the Mixed μ Problem," *1992 American Control Conference*, Chicago, USA, 1992, pp. 2190–2194. https://doi.org/10.23919/ACC.1992.4792521.

[37] Theis, J., Pfifer, H., and Seiler, P., "Robust Modal Damping Control for Active Flutter Suppression," *Journal of Guidance, Control, and Dynamics*, Vol. 43, No. 6, 2020, pp. 1056–1068. https://doi.org/10.2514/1.G004846.

[38] Seiler, P., Packard, A., and Gahinet, P., "An Introduction to Disk Margins [Lecture Notes]," *IEEE Control Systems Magazine*, Vol. 40, 2020. https://doi.org/10.1109/MCS.2020.3005277.

[39] Young, P. M., "Controller Design with Real Parametric Uncertainty," *International Journal of Control*, Vol. 65, No. 3, 1996, pp. 469–509. https://doi.org/10.1080/00207179608921707.

[40] Bennani, S., Looye, G., and Mulder, J. A., "RCAM Design Challenge Presentation Document: the μ-Synthesis Approach," Technical report TP-088-11, GARTEUR, 1997.

[41] Balas, G., Chiang, R., Packard, A., and Safonov, M., "Robust Control Toolbox User's Guide," Software Package Documentation, MATLAB R2024b, MathWorks Inc., 2024.

[42] Schmidt, T.G., et. al., "Assessing Sensor-Model-Fusion Technologies on a Flexible Aeroelastic Wing Demonstrator through Wind Tunnel Testing in the DLR Project SAFER^2," *Deutscher Luft- und Raumfahrtkongress (DLRK)*, DGLR, Augsburg, Germany, 2025. https://doi.org/tobepublished.

[43] Dillinger, J., Mai, H., Krüger, W. R., Schmidt, T. G., and Stalla, F., "Design, Manufacturing and Identification of an Actively Controlled Flexible Wing for Subsonic Wind Tunnel Testing," *International Forum on Aeroelasticity and Structural Dynamics (IFASD 2024)*, Den Haag, The Netherlands, 2024. URL https://elib.dlr.de/205840/.

[44] Schmidt, T. G., Dillinger, J., Ritter, M., Altkuckatz, A., Hanke, C., Braune, M., Krüger, W. R., and Mai, H., "Design and Experimental Characterization of a Gust-Generator Concept with Rotating-Slotted Cylinders in the Low-Speed Wind Tunnel DNW-NWB," *International Forum on Aeroelasticity and Structural Dynamics (IFASD 2024)*, Den Haag, The Netherlands, 2024. URL https://elib.dlr.de/205804/.

[45] Stein, G., "Respect the Unstable," *IEEE Control Systems Magazine*, Vol. 23, No. 4, 2003, pp. 12–25. https://doi.org/10.1109/MCS.2003.1213600.